RIVISTA DEL NUOVO CIMENTO Vol. 39, N. 5 2016
DOI 10.1393/ncr/i2016-10123-5

X-ray and simulation studies of water(*)

A. Nilsson(1)(2)(3), D. Schlesinger(3) and L. G. M. Pettersson(3)

(1) *SUNCAT Center for Interfacial Science and Catalysis*
SLAC National Accelerator Laboratory
Menlo Park, CA 94025, USA
(2) *Stanford Synchrotron Radiation Lightsource, SLAC National Accelerator Laboratory*
Menlo Park, CA 94025, USA
(3) *Department of Physics, AlbaNova University Center, Stockholm University*
SE-10691 Stockholm, Sweden

Summary. — Here we present a picture that combines discussions regarding the thermodynamic anomalies in ambient and supercooled water with recent interpretations of X-ray spectroscopy and scattering data of water. At ambient temperatures most molecules favor a closer packing than tetrahedral, with strongly distorted hydrogen bonds, which allows the quantized librational modes to be excited and contribute to the entropy, but with enthalpically favored tetrahedrally bonded water patches appearing as fluctuations, *i.e.* a competition between entropy and enthalpy. Upon cooling water the amount of molecules participating in tetrahedral structures and the size of the tetrahedral patches increase. The two local structures are connected to the liquid-liquid critical point hypothesis in supercooled water corresponding to high-density liquid (HDL) and low-density liquid (LDL). We demonstrate that the HDL local structure deviates from a tetrahedral coordination not only through a collapse of the 2nd shell but also through severe distortions around the 1st coordination shell.

(*) Reproduced from *Proceedings of the International School of Physics "Enrico Fermi"*, Course 187, *Water: Fundamentals as the Basis for Understanding the Environment and Promoting Technology*, edited by P. G. Debenedetti, M. A. Ricci and F. Bruni (IOS Press, Amsterdam and SIF, Bologna) 2015, pp. 77-135.

1. – The inhomogeneous structure hypothesis

The understanding of the structure and dynamics of the hydrogen-bonding (H-bonding) network in water is essential for many problems in chemistry, physics, biology and geoscience. Water is not only important but also has many quite unusual properties such as increased density upon melting, decreased viscosity under pressure, density maximum at 4 °C, high surface tension and many more [1]. Water properties are also affected by various solutes and are fundamental to biological activity [2, 3].

In the low-temperature regime, below the freezing point, these properties deviate particularly strongly from those of a normal liquid. Although the anomalies are extreme in the supercooled region they are also present at ambient conditions where most of waters' physical, chemical and biological processes occur. Here we will focus on thermodynamic response functions that depend on fluctuations in various properties [4]. One example (fig. 1a) is the isothermal compressibility, κ_T, related to volume, or equivalently density, fluctuations in the liquid. κ_T decreases upon cooling as for a normal liquid, but only down to 319 K (46 °C). At this temperature κ_T exhibits a shallow minimum and upon further cooling starts to increase again, indicating that density fluctuations in the liquid increase as thermal energy is removed. Another example is the isobaric heat capacity, C_P, which is related to entropy fluctuations [5] and below 308 K (35 °C) also this property of water shows an anomalous increase compared to normal liquids (fig. 1b). The thermal expansion coefficient, α_P, which is related to the cross-correlation between fluctuations in density and entropy, becomes negative for water below the density maximum at 277 K (4 °C) (fig. 1c).

Characteristic for all three is that they are related to fluctuations in the liquid and that these *increase* upon cooling contrary to expectation for normal, simple liquids. Importantly, while these fluctuations and apparent divergences of thermodynamic response functions are most evident when water is supercooled below the melting point

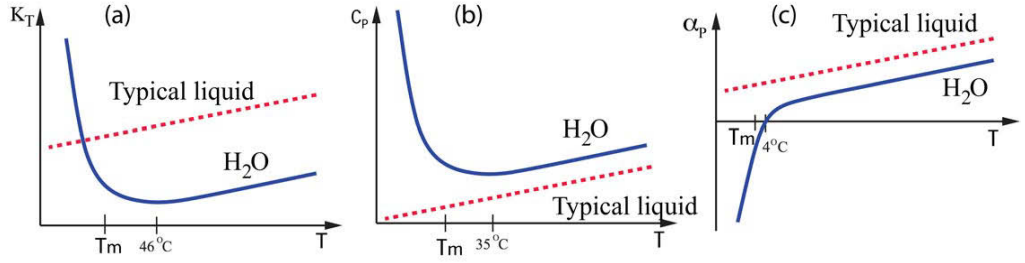

Fig. 1. – Comparison of thermodynamic response functions for H_2O water (full line) with that of typical liquids (dashed line) showing the onset of anomalous behavior already at ambient temperatures and pressure. The melting point is indicated by Tm. (a) Isothermal compressibility, κ_T, which shows a minimum at 319 K (46 °C), (b) isobaric heat capacity, C_P, with minimum at 308 K (35 °C) and (c) coefficient of thermal expansion, α_P, which becomes negative at 277 K (4 °C). (Figure adapted from ref. [6].)

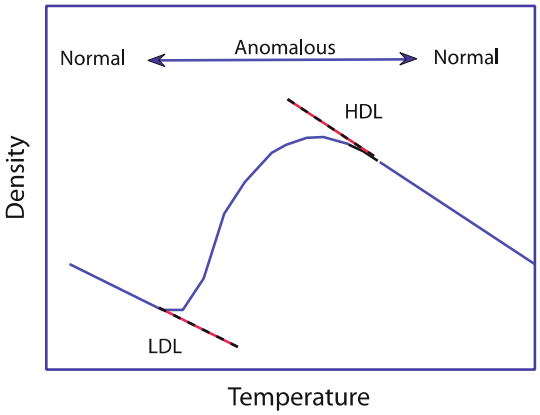

Fig. 2. – Hypothetical temperature-dependent density variation in water divided into two normal liquid regions and one anomalous region in between. The anomalous region curve is taken from a TIP4P/2005 simulation study [11].

273 K (0 °C) [4,7-9], they start to influence water properties already in the ambient, biologically relevant regime and grow in importance in a continuous, but rapidly increasing fashion as thermal energy is removed.

Figure 2 shows a hypothetical variation of the density of water from hot temperatures down deep into the supercooled region. This curve is consistent with measured data of water ranging from hot temperatures and down to roughly 240 K showing the density maximum and the initial part of the decline of the density with decreasing temperature [10] whereas the full curve has been obtained in simulations using the TIP4P/2005 model [11] and for water in nanoconfinement [12]. We distinguish three different regions where water in both the hot and extremely cold regions corresponds to a normal liquid with the anomalous region in between. The deviation of the thermodynamic response functions as shown in fig. 1 occurs upon entering into the anomalous region. This corresponds to

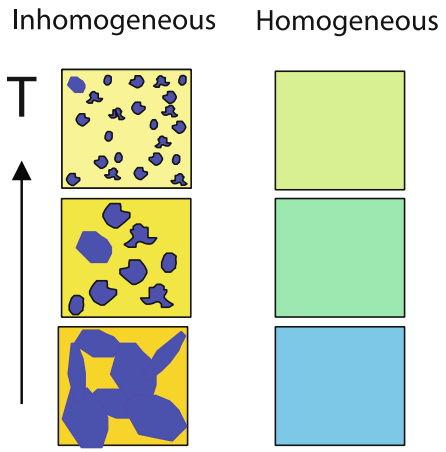

Fig. 3. – Schematic picture of two hypothetical continuous water models with either a homogeneous distribution of local structures (indicated on the right) or a bimodal inhomogeneous distribution that varies with temperature (left). The yellow region indicates HDL local structures and the blue corresponds to LDL for the inhomogeneous model whereas the homogeneous is an average of the two local structures. Note that the boundary between the two types of regions in real water is expected to be less sharp.

temperatures where the density starts to deviate from a linear relationship and where the isothermal compressibility and the heat capacity pass through a minimum and instead rise upon further cooling, as seen in fig. 1. This should be around 315 K [13] meaning that water at the important ambient temperature is already in the anomalous region.

Fitting neutron scattering data of water at various pressures and temperatures has allowed the determination of pair-correlation functions corresponding to two extreme states of liquid water [14], high-density liquid (HDL) and low-density liquid (LDL). The latter corresponds to a tetrahedral structure similar to what is seen in ice whereas the former is characterized by a collapse of the tetrahedral structure allowing for higher density with also some distortions in the H-bonding in the first coordination shell [15-18]. The LDL structure is mostly driven by the directional strong H-bonding while the HDL structure is more due to the isotropic van der Waals interaction [19] that leads to a collapse of the tetrahedral structure and implies a local structure more towards a hexagonal arrangement [20].

The normal liquid regions at high and low temperatures are dominated by structures resembling either HDL or LDL. They have a normal behavior of increasing density with decreasing temperature as expected from any liquid. The anomalous region is where the liquid structure is transforming from a HDL to a LDL dominated structure. This is a continuous transition occurring over a large temperature range. The presence of a density maximum and minimum seen in fig. 2 becomes obvious with the transition from one type of normal liquid with higher density to one with lower density when also each normal liquid changes density with temperature.

We can envision two extreme situations regarding the structure of the liquid in the anomalous region, illustrated in fig. 3; both are continuous on a larger scale, but locally either inhomogeneous or homogeneous. The first corresponds to the locally inhomogeneous model with the above described two classes of local structural extremes that are

either HDL-like or LDL-like and form spatially separated local regions on temperature dependent length and time scales [11, 13, 15-17, 21-27]. The HDL-like structure, with thermally excited librational modes, dominates at high temperature and is continuously changing with temperature to become less disordered upon cooling as these modes become less excited. Additionally, with decreasing temperature, there appear patches of the LDL-like structure through collective fluctuations. These patches, where the molecules are bonded with strong tetrahedral bonds which make thermal excitation of librational modes unfavorable, have a size of the order of around 1 nm at ambient temperature and grow in size upon cooling [15]. In comparison to the HDL structure the LDL patches show less variability with temperature in terms of local structure since disorder due to librational excitations is largely absent. The homogeneous model on the other hand is also continuous but now no additional patches appear [28, 29]. It has been argued that it is more of a structural average of the HDL and LDL regions with no specific local structures but more ordered in a tetrahedral arrangement than the HDL while less strongly tetrahedral compared to LDL [23]. Here both models are continuous but with the difference that in the inhomogeneous structure model there are fluctuations where local, structurally highly ordered tetrahedral patches appear on specific length and time scales. We will in the following in particular argue that it is only the inhomogeneous structure model that can explain the transition of the liquid properties with temperature in the anomalous region as well as the experimental X-ray spectroscopy and scattering data.

The hypothesis can be extended into the supercooled region where such fluctuations increase anomalously and can explain the enhancements of the thermodynamic response functions shown in fig. 1. These observations are consistent with the proposed liquid-liquid critical-point (LLCP) [30, 31] terminating the coexistence curve separating two macroscopic states of the liquid, HDL and LDL, in deeply supercooled and pressurized water. However, it is not yet entirely clear where the critical point would lie in terms of pressure [32, 33]. There are also theoretical investigations indicating that the liquid is not in metastable equilibrium under deeply supercooled conditions, but instead ice would form on a timescale faster than the liquid can be equilibrated [34, 35]. In contrast, several recent studies do find an equilibrated metastable LDL [36-39].

In this contribution we will go through various arguments for the inhomogeneous model based on the temperature dependence of the thermodynamic response functions. We will present spectroscopy measurements based on the electronic structure of the water molecule with an emphasis on the unoccupied orbitals and water vibrations followed with interpretations based on trends and theoretical simulations. Finally we bring forward X-ray and neutron scattering experiments together with various interpretations.

Ceci n'est pas une pipe

Before discussing experimental data and their representation in molecular dynamics (MD) simulations we would like to remind the reader of The Treachery of Images by Magritte showing the image of a pipe with the sentence "This is not a pipe" below it. Similarly, MD simulations of water are but models of the liquid and, although the model can be very accurate in many respects, it should not be confused with the real liquid. In the present section and elsewhere we thus consistently use the terminology of real water for experimental results and, *e.g.*, SPC/E water and TIP4P/2005 water to distinguish between the representation of water and the real liquid.

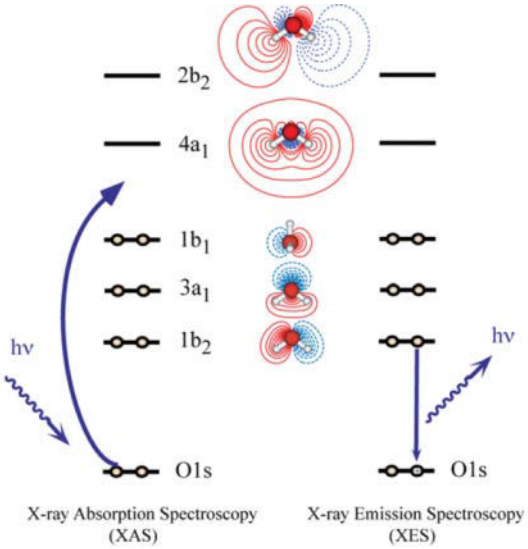

Fig. 4. – Schematic orbital diagram of a free water molecule illustrating the principles for X-ray absorption and emission spectroscopy.

2. – Two local distinct structures

Here we will discuss the evidence for the inhomogeneous structure based on spectroscopic detection of water in two classes of local environments using X-ray spectroscopy and infrared (IR) and Raman spectroscopy. Let us first focus on the application of X-ray spectroscopy to water that has developed over the past decade with X-ray absorption spectroscopy (XAS) [3, 18, 40], X-ray Raman scattering (XRS) [41] where the energy-loss of high-energy photons is measured which, in the small momentum transfer limit, becomes almost identical to XAS [3] and X-ray emission spectroscopy (XES) [23, 42-44].

2˙1. *X-ray spectroscopy.* – Figure 4 shows a molecular orbital diagram of the free water molecule [3] relevant for our discussion of XAS/XRS and XES. The three outermost occupied orbitals are the bonding $1b_2$ and $3a_1$ and the non-bonding $1b_1$ lone-pair. To the two bonding orbitals corresponds a set of orthogonal orbitals of antibonding character which are denoted $4a_1$ and $2b_2$ and which are unoccupied in the ground state. Figure 4 illustrates the two X-ray spectroscopies through a process where an electron is either excited from the O $1s$ core orbital to the unoccupied orbitals or an electron decays from the occupied orbitals into the O $1s$ core-hole created in a preceding absorption event. The former is X-ray absorption where a photon is absorbed. The same excitation can occur through X-ray Raman scattering in which instead a high-energy photon undergoes an energy loss where the energy is given to the excitation process from the O $1s$ to the unoccupied states. The decay of the excited state illustrated in fig. 4 is the X-ray emission process where a photon is emitted with energy corresponding to that released from the decay process.

One thing that we immediately note in fig. 4 is the large difference in spatial extent between the occupied and unoccupied orbitals. The occupied orbitals are more confined to the close proximity of the molecule whereas the unoccupied orbitals have larger spa-

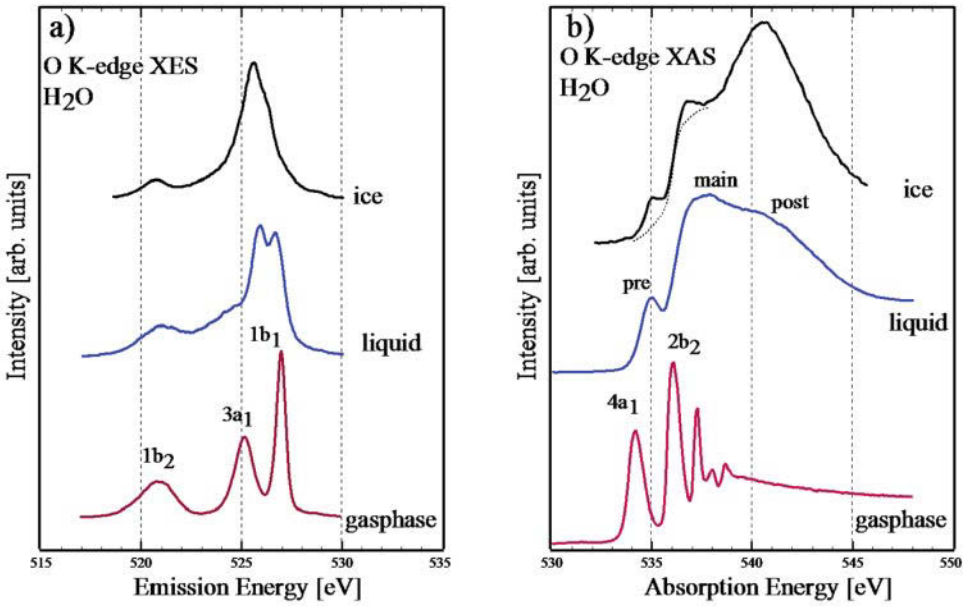

Fig. 5. – (a) X-ray Emission Spectra (XES) [23,45,46] at non-resonant conditions and (b) X-ray Absorption Spectra (XAS) [3] of the three different aggregation forms: gas phase, liquid and crystalline ice. The dotted lines in the ice spectrum indicate the likely spectrum in the absence of structural defects.

tial extent, in particular around the hydrogen atoms. This results in a large difference in sensitivity to H-bonding between the two spectroscopies. Figure 5 shows XES and XAS spectra of gas phase, liquid and ice [3, 23, 45, 46]. The XAS spectrum changes dramatically due to H-bonding when other molecules come close and overlap between the unoccupied orbitals causes rehybridization and energy shifts. On the other hand, the occupied orbitals will be much less sensitive to H-bonding since the overlap with other molecules is much smaller. This is also observed in most parts of the XES spectra of water [23, 42, 43, 47] and also in the corresponding photoelectron spectra where the valence electrons are directly ionized [48-50]. In the XES spectra the interesting split in the $1b_1$ orbital, as shown in fig. 5, is mainly due to a core level shift of the O $1s$ due to differences in local H-bonding which will affect the energy of the decay [23] since it is a measure of the difference in the total energy between a hole in the O $1s$ level and a valence hole.

One of the most essential aspects of the spectroscopic process is that it provides an atom-specific probing of the electronic structure around a specific site coupled with the dipole selection rule. This comes from the unique property to probe the valence electrons close to the core electron shell where the matrix element in the X-ray transition becomes atomic-like. It forms the basis for the "one-center approximation". The intensity of the X-ray transition is thus directly related to the partial population of atomic $2p$ character in the different occupied and unoccupied molecular orbitals [3]. Furthermore, the attosecond time scale of the XAS/XRS excitation/scattering process and the O $1s$ life time of around 4 fs in XES [51] are much shorter than the 100 fs to 1 ps for H-bond dynamics [52]. The spectra thus correspond to an instantaneous sampling of effectively frozen configurations as is also the case in X-ray scattering or X-ray diffraction.

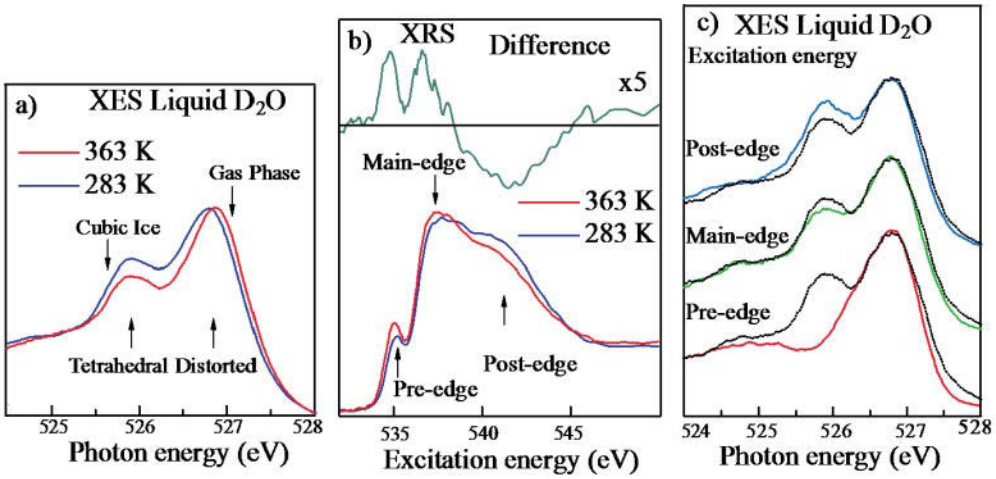

Fig. 6. – (a) The lone-pair $1b_1$ region of the O $1s$ soft X-ray emission spectra of liquid D_2O at 283 and 263 K using a non-resonant excitation energy of 550 eV. The positions of the corresponding $1b_1$ state of crystalline ice and gas phase water are indicated with arrows [23]. The spectra were normalized to give the same peak height of the distorted component. (b) X-ray Raman scattering spectra of liquid H_2O at 283 and 363 K normalized to have the same area and the difference between the two spectra magnified by a factor of 5 [15]. (c) XES spectra at various excitation energies (full lines) compared to non-resonant excitation (dotted black lines) at 550 eV of D_2O water at 298 K [15]. Note that the pre-edge excited spectrum has been shifted by 0.45 eV to compensate for the spectator shift of a localized excited intermediate state [64].

Figure 6a shows the temperature dependence in the lone-pair $1b_1$ region of the XES spectrum for D_2O [23]; using the heavier isotope minimizes core-hole induced vibrational interference effects on the spectral line shape and the two peak heights are therefore different compared to the split peak in H_2O shown in fig. 5 (left) [23, 42, 53, 54]. The spectra show a split of the $1b_1$ lone-pair into two peaks, with one close in energy position to the $1b_1$ in crystalline ice and the other to $1b_1$ in water vapor [23]. The two peaks can thereby be related to tetrahedral and H-bond distorted local structures as supported also by increasing temperature converting tetrahedral $1b_1$ to distorted $1b_1$ [23]. This is the clearest evidence of two different structural motifs obtained in any spectroscopic studies in the literature since two well resolved peaks are directly observed.

Let us now turn to the probing of the unoccupied states. Figure 6b shows the temperature-dependent XRS spectra [15]. The sensitivity of the spectroscopy to the change of H-bond topology, as shown here with temperature variation, is well established experimentally [3]. In particular, it can be shown that the pre- (535 eV) and main-edge peaks (537 to 538 eV) fingerprint distorted H-bonds, whereas the post-edge (540 to 541 eV) is associated with strong H-bonds and is further enhanced for tetrahedral H-bond structures [3, 55].

2˙2. *Connecting XAS/XRS and XES.* – We use energy-selective excitation to make a connection between the two X-ray spectroscopies. The XES spectra shown in fig. 5a and 6a were all taken with excitation at 550 eV, well beyond the region with structure-dependent spectral features in the XAS spectrum. Tuning instead the energy to the

specific resonant features (pre-, main- and post-edge) in the absorption spectrum makes a connection between the two X-ray spectroscopies by selecting the corresponding structural species for XES [23]. This is shown in fig. 6c where resonant XES spectra are compared with non-resonant (550 eV) XES. Normalizing the intensities to the distorted peak, we find that pre-edge excitation essentially eliminates the tetrahedral peak (red); this shows directly that the pre-edge in absorption is unique for molecules contributing to the distorted $1b_1$ peak in emission, as will be discussed further below. Excitation on the main edge gives a slight enhancement of the distorted (green), while excitation on the post-edge instead enhances the tetrahedral peak compared to the distorted (blue). Since the absorption post-edge feature in ice is much stronger than in the liquid [18], the resonant XES (blue) is consistent with the low-energy peak being related to tetrahedral-like species. The pre-edge peak in XRS is assigned to distorted H-bonding configurations [18, 40, 56-60]. This assignment is fully consistent with the experimentally observed temperature dependence of both XRS and XES. In XRS, the post-edge decreases and the pre-edge increases with increasing temperature (see fig. 6b), similar to the post-edge-associated tetrahedral peak converting to the pre-edge-associated distorted peak in XES. Hence, both XES and XRS indicate in a consistent manner that water consists of two distinct, interconverting structural species in a ratio that depends on temperature. This is also within the range of possible structures that X-ray and neutron diffraction data allow, as shown in recent analyses using reverse Monte Carlo (RMC) modeling [61, 62] and from fitting pressure and temperature dependent neutron diffraction data [63].

2˙3. *Peak shifts with temperature.* – There is another important temperature effect in the XES and XRS spectra indicating changes beyond the interconversion of the two structural species. The distorted peak in XES (fig. 6a) shifts towards higher emission energy with increasing temperature whereas the tetrahedral peak is at fixed energy [15, 23]. Let us now take a closer look at the XRS high-resolution spectra of water at temperatures of 4, 22, 60 and 90 °C shown in fig. 7a [3, 15] where also another group has obtained similar data [65]. We observe the same trend as in fig. 6b with an increase in pre-edge and main-edge and decrease in post-edge intensities with increasing temperature. However, there is some additional information similar to the XES data. First we note that there is no additional broadening of the pre-edge peak with increasing temperature. This implies that the structure that gives rise to the pre-edge feature is still relatively well defined although disorder due to temperature must be present. The top part of fig. 7a shows difference spectra with respect to room temperature. We observe an energy shift to lower energy towards the gas phase values of the $4a_1$ and $2b_2$ spectral peaks and enhanced intensity of both the pre-edge and the main-edge features with increasing temperature in the difference spectra. This implies that the distorted structural species successively becomes more distorted with increasing temperature through thermal excitation weakening the H-bonding whereas the tetrahedral-like species do not significantly change their H-bonding. The conversion of tetrahedral-like to distorted local H-bonding situations with temperature shows that the tetrahedral-like component is of lower energy. The shifting of the distorted peak position in XES and the pre-edge and main-edge in XRS with temperature indicate an increase in entropy of the distorted component as it becomes thermally excited [15]. All of these observations are consistent with the fact that the tetrahedral structure is of lower energy - lower entropy and the distorted structure of higher energy - higher entropy.

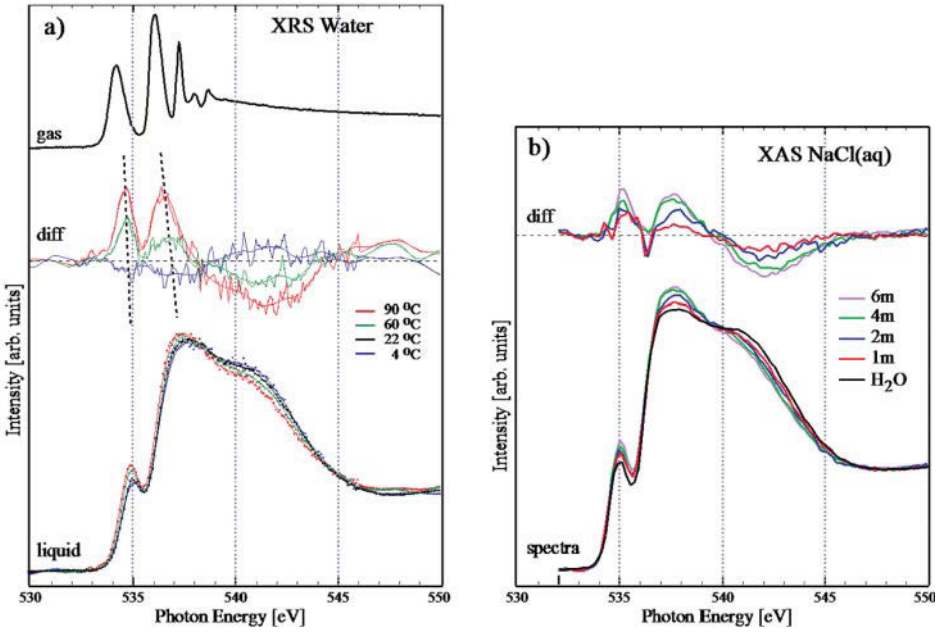

Fig. 7. – (a) Bottom: O K-edge XRS spectra for liquid water H_2O at various temperatures (4,22,60, and 90 °C) [15] (middle) Difference spectra relative to the room temperature spectrum (22 °C). Help lines are used to illustrate the shift of the pre-edge and main-edge towards lower energies. Top: The FY-XAS spectrum of gas-phase H_2O is shown for comparison. All spectra are on a common energy scale where the $3p$ Rydberg state of the gas-phase spectrum is calibrated to 537.25 eV. (b) XAS spectra of NaCl solutions with increasing concentration measured in transmission mode, compared with the spectrum of pure water [3]. The difference spectra are shown at the top of the figure.

2˙4. *Comparing effects of temperature with adding salts*. – Figure 7b shows transmission XAS spectra of pure water and 1–6 molal NaCl solutions with difference spectra with respect to pure water shown in the top part of the figure [3, 66]. We clearly see an increase in the pre-edge and main-edge and decrease of the post-edge features with increasing concentration. Based on the spectral changes this would imply that for NaCl solutions we have a conversion of tetrahedral to distorted local structures as has also been suggested from MD simulations [67, 68]. At first glance, the general trend of the spectral changes, shown in the difference spectra, *i.e.* the spectra of aqueous solutions minus the spectrum of pure water, seems similar to the changes caused by a temperature increase as shown in fig. 7a. However, upon closer inspection a significant difference can be observed between the effect of temperature increase and NaCl solvation, *i.e.* there is no pre-edge or main-edge shift with increasing NaCl concentration. Therefore, in the case of NaCl solvation, the distorted species are converted from tetrahedral species without introducing additional thermal energy to the system, consistent with the increased pre-edge being located at the same energy position as at 25 °C H_2O.

2˙5. *Consistency with vibrational spectroscopy*. – IR and Raman spectroscopy of the OH stretch region have been the main spectroscopic tools to investigate water for many years. Although this topic is complicated and many different interpretations have been

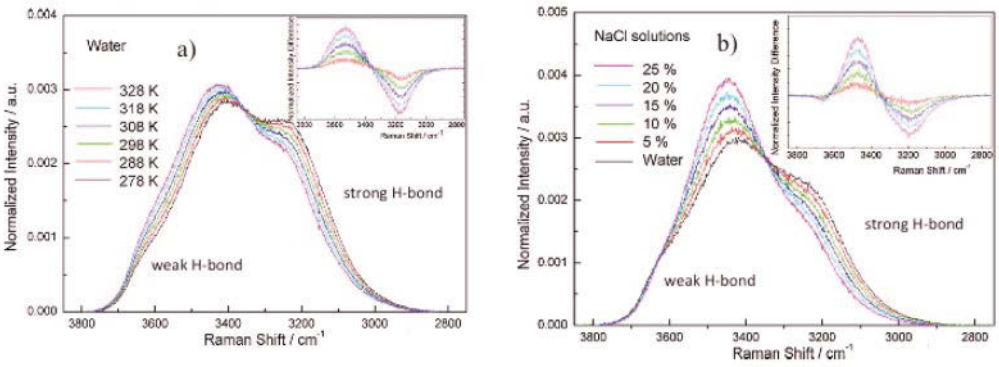

Fig. 8. – (a) The Raman OH stretching band of water at various temperatures from 5 to 55 °C [71]. (b) The Raman OH stretching band of NaCl solutions [71]. The inserts in a) and b) show the normalized difference spectra.

given [59, 69-78] here we only want to point to the consistency between what is experimentally observed through vibrational Raman spectroscopy and XAS. In the case of XAS we probe the excitation spectrum around each O atom in its local environment whereas in Raman spectroscopy the stretch frequency of OH groups in their local surrounding is probed. Here we will focus on the pure H_2O data and not the typical dilute HDO in either H_2O or D_2O. In particular since D_2O forms stronger H-bonds than H_2O [1] we cannot assume that an HDO molecule as an impurity in, *e.g.*, H_2O gives a reliable picture of the distribution of configurations available to the majority species (H_2O) in the liquid. Indeed, both from experiment and simulations a preference for exposing OH rather than OD of HDO at the interface between liquid and gas phase has been found [79, 80]. Furthermore, recent XES measurements focusing on pre-edge excitation demonstrate a preference for the OH group being non-H-bonded in distorted HDL-like species involving HDO; this is also supported by path integral (PIMD) simulations [81]. Thus, in particular if there are two distinct species with asymmetric respectively symmetric H-bonding, the asymmetry of HDO might generate a bias for probing preferentially the asymmetric HDL-like species.

Figure 8 shows a similar comparison between temperature and NaCl induced effects on the Raman OH stretch spectra [71] as in the case for XAS/XRS in fig. 7. We observe that the 3200 cm^{-1} feature drops in intensity whereas the 3450 cm^{-1} peak increases in intensity both with increasing temperature and with NaCl concentration similarly to the decrease of post-edge and increase of the pre- and main-edges in XAS/XRS. We can thereby propose that the 3200 cm^{-1} feature is related to tetrahedral structures while the 3450 cm^{-1} peak is connected to the distorted species. For asymmetrical water species with the case that the two donor H-bonds have different strengths, we should expect to see two distinct frequencies. Since most likely there is a distribution of H-bond strengths for the distorted species we expect a broad range of frequencies related to the region 3400–3700 cm^{-1}. Similarly as in XAS/XRS, where the pre- and main-edges shift with increasing temperature, but not with increasing NaCl concentration, the Raman spectra show a blue-shift of the 3400–3700 cm^{-1} region with increasing temperature but stays at fixed energy for the NaCl induced effects. The observations from temperature and salt effects on XRS/XAS and the Raman OH stretch are thus fully consistent with the two-species hypothesis.

The OH stretch frequency is indirectly affected by external H-bonding since the covalent internal OH bond gets weaker. In the low-frequency regime there are collective modes related to vibrations in the H-bonding network. Recently, in an investigation of the vibrational dynamics and relaxation processes using time-resolved optical Kerr spectroscopy it was demonstrated that there are signatures of two different species in water [26]. In particular modes related to intermolecular stretch vibrations for tetrahedrally arranged water molecules were observed at $225\,\mathrm{cm}^{-1}$ and for water molecules in distorted H-bond arrangements at $180\,\mathrm{cm}^{-1}$, respectively. These interconvert upon cooling from ambient to supercooled temperatures where the intensity for the tetrahedral component increases.

In accordance with the small tetrahedral peak in XES, the relatively weak post-edge in XAS/XRS and smaller intensity in the Raman $3200\,\mathrm{cm}^{-1}$ region, also the $225\,\mathrm{cm}^{-1}$ feature has less intensity at ambient temperatures. This indicates the distorted species to be the dominant structural arrangement at room temperature. The tetrahedral components grow upon cooling, with the growth expected to become accelerated deep in the supercooled regime.

3. – The nature of the distorted species; understanding XAS/XRS

Here we will discuss the nature of the distorted species and if they can be related to the hypothesis of HDL with a more compact coordination shell but with molecules both at longer and shorter distances leading to breaking of H-bonds in comparison to the tetrahedral network. We will focus on the XAS/XRS spectra since the three spectral features pre-, main- and post-edges are related to different interactions in the liquid. We have already demonstrated in the previous section that the post-edge is connected to H-bonds and becomes particularly enhanced for tetrahedral structures but the question is what affects the pre- and main-edges?

3˙1. *The pre-edge.* – Let us turn to some experimental model systems using two-dimensional water overlayers on surfaces and also high-pressure ices to shed light on how the spectral features are related to the H-bonding structure. Due to the directionality of the H-bond and the fact that X-rays produced as synchrotron radiation can be linearly polarized, it is particularly advantageous to study the H-bond environment in lower dimensions where the X-ray E-vector can be aligned to selectively probe the in-plane H-bond interactions. The changes in the electronic structure due to the chemical bonding to the substrate are mainly observed in the out-of-plane orientation of the E-vector [82].

The adsorption and structural growth of water on Ru(0001) has been characterized with a number of different surface science techniques such as scanning tunneling microscopy (STM) [55], infrared reflection absorption spectroscopy (IRAS) [83] and X-ray photoelectron spectroscopy (XPS) [84]. At low coverage and very low temperatures water adsorbs as isolated molecules far away from other molecules. As the coverage increases the molecules nucleate into small clusters in which each molecule has its plane near-parallel to the surface. The smallest clusters are hexagonal rings. In the smallest rings or at the periphery of the larger clusters the molecules are in an asymmetrical H-bonding configuration with one OH-group involved in H-bonding while the other is a free non–H-bonded OH-group parallel to the surface. As the coverage increases further the clusters increase in size and eventually coalesce into a two-dimensional overlayer where all in-plane H-bonds are saturated.

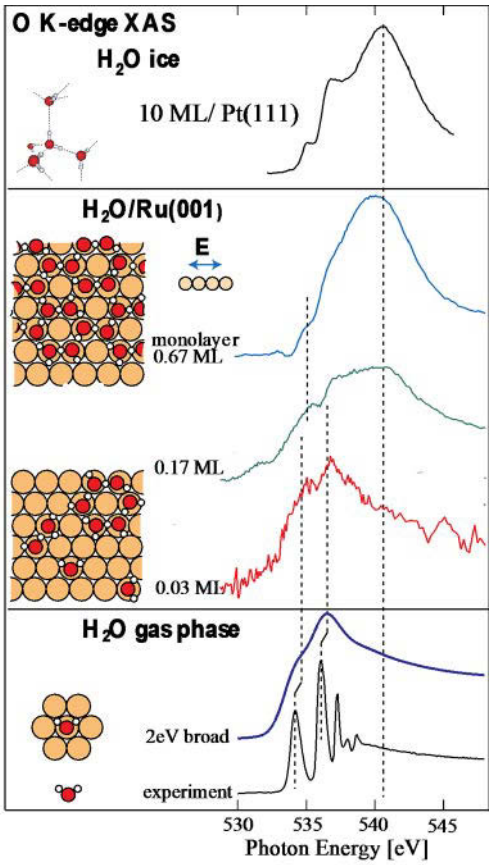

Fig. 9. – Left: Schematic illustrations of water at various coverages on Ru(0001) from low coverage with individual water molecules, intermediate coverage where small clusters are formed with asymmetrical H-bonding at the edges and the complete monolayer where nearly all H-bonds are saturated in the plane parallel to the surface [3, 55]. Right: XAS spectra measured with the E-vector in-plane with respect to the surface of water adsorbed on Ru(0001) at different coverages deposited and measured at 37 K except for the monolayer coverage which was annealed to 150 K and measured at 100 K [3,55]. Spectra of gas phase and ice are shown as comparison [40, 85].

Figure 9 shows the experimental O 1s XAS spectra from low-coverage water up to a completed monolayer with the E-vector of the exciting photon in-plane to interrogate specifically the two-dimensional H-bond network [55]. For comparison, we show the X-ray absorption spectrum from hexagonal ice [85] and gas-phase water [40], with guidelines for the energy positions of the molecular gas-phase $4a_1$ and $2b_2$ orbitals as well as for the strong post-edge in ice. In the low-coverage phase (0.03 ML), corresponding to mobile [86] monomer water, a comparison with the gas-phase spectrum broadened by 2 eV indicates spectral features associated with the gas-phase molecular orbitals also for the molecules at the surface. The spectrum becomes broadened and shifted in energy due to variations in local geometry and coupling to the conduction band of the metal. There is no distinct post-edge feature in the spectrum and most of the intensity is at lower energy

similar to the gas-phase. As the coverage increases clusters form and we can see the effects of H-bonding in the X-ray absorption spectra. From an H-bonding perspective, the water molecules in the clusters have a high asymmetry with one strong donor H-bond and one OH-group pointing along the in-plane direction away from the cluster. We see significant intensity in the post-edge region above 540 eV, which was not present at the low coverage. We also note that a rather well-defined pre-edge peak emerges at an energy intermediate of the gas-phase $4a_1$ and $2b_2$ peaks. Upon completion of the monolayer, the post-edge becomes even more intense whereas the pre-edge diminishes and almost disappears compared to the dominating post-edge; the spectrum gains a strong resemblance with the spectrum of bulk ice.

It is clear from the spectra in fig. 9 that the post-edge can be associated with the presence of H-bonds in either asymmetric or symmetric species. The monolayer spectrum is rather similar to the ice spectrum except for the width of the post-edge and the missing sharp pre-edge. The overlayer has a better completed H-bond network without the structural defects in the form of higher-density amorphous structures present in bulk ice samples. The remaining faint pre-edge feature can be related to vibrational motions that break the symmetry [87].

In the free water molecule, the $4a_1$ and $1b_2$ orbitals are delocalized over both OH groups due to the C_{2v} symmetry. The appearance of the pre-edge feature for asymmetrically H-bonded species is a result of localization of the OH antibonding orbital onto the free or weakly donating OH-group [3, 18, 64, 88]. In order to generate a localized orbital on the free OH-group it is necessary to mix the gas phase $4a_1$ and $1b_2$ orbitals [88]. This then results in a pre-edge feature at an energy position that appears in between the two gas-phase orbitals. Thus the appearance of the pre-edge feature as a localized orbital on the non–H-bonded OH group in the spectra from the small clusters is fully consistent with the interpretation in terms of the asymmetrical single-donor (SD) species. We note here that also the liquid water pre-edge feature is in between the $4a_1$ and $1b_2$ spectral features in the gas phase as shown in fig. 5b.

This model system seems to give evidence that the pre-edge feature is related to broken or weakened H-bonds and the post-edge to strong H-bonds that are typically found in ice. Other model systems such as the ice surface [3,85], glycine on Cu(110) [89-92], water on Cu(110) [93] and the mixed OH-H_2O layer on Pt(111) [94] support this interpretation.

Recently, a detailed analysis of individual H-bond strengths of molecules in an *ab initio* MD simulation revealed instantaneous asymmetries between strong and weak H-bonds on the same molecule and it was found that these interchange due to H-bonding fluctuations with the surroundings [95]. Furthermore, it was confirmed that the distinct pre-edge and main-edge features of the XAS spectra originate from molecules with high instantaneous asymmetry. In real water the asymmetry, seen in terms of a few tenths of Å in the simulation, is most likely larger since the simulation was extremely overstructured as seen from the O-O pair-correlation function (see sect. **7**). This has also been suggested based on spectrum calculations from specific structures in *ab initio* MD simulations [57]. Here we can conclude, based on the experimental model systems and simulations, that the pre-edge feature is connected to distortions leading to a weak H-bond in asymmetrical structures. What about the main-edge which is the strongest spectral feature in the water spectrum?

3˙2. *The main edge.* – Recently, an important XRS study was conducted on high-pressure crystalline ices up to a density of 1.60 g/cm^3 [96]. Figure 10a shows the XRS spectra of hexagonal ice (I_h) and three different high-pressure crystalline ices [3]. We

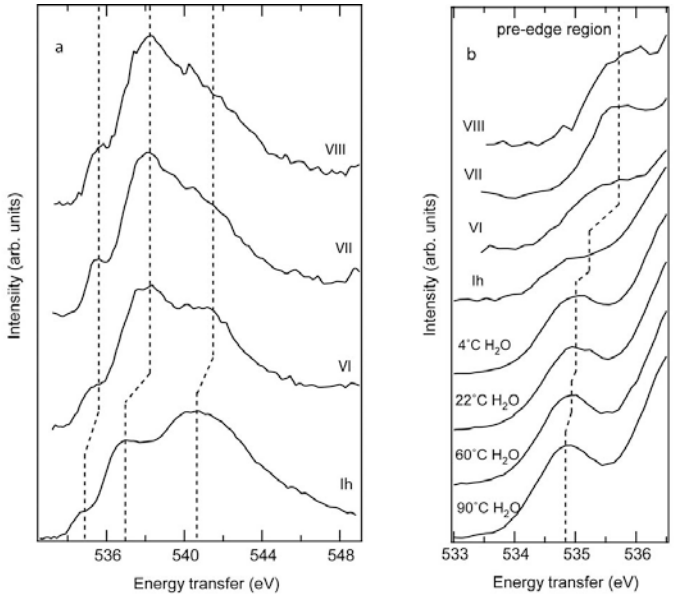

Fig. 10. – Oxygen XRS spectra of ices I_h and VI-VIII. (a) XRS spectra at small momentum transfer, lines mark (1) pre-edge, (2) main edge, and (3) post-edge positions [96]. (b) Enlarged region around the pre-edge with the addition of temperature dependent water XRS spectra. The alignment of the energy scale between the two experimental data sets of water and ice is based on that the absolute energy of the liquid was calibrated against the gas phase and the hexagonal ice spectrum was calibrated absolutely in a previous XAS study of ice using the difference between 1st- and 2nd-order soft-X-ray light [3]. The energy scale of the ice XRS spectra was then aligned with respect to the energy calibration of the XAS hexagonal ice spectrum.

directly observe that there are quite distinct changes in the spectra with increasing density. In particular the main-edge spectral feature grows in intensity in comparison to the post-edge. Additionally there are also increases in the pre-edge intensity. What is in particular different in terms of structure for the high-pressure ices is the collapse of the 2nd shell from the tetrahedral distance of 4.5 Å to much shorter distances where eventually it moves close enough to form two interpenetrating sublattices. Figure 11 shows the main-edge–to–post-edge intensity ratio as a function of 2nd shell distance and density for the different ices and for water [96]. It is most interesting that the main-edge–to–post-edge ratio for water would indicate a 2nd shell distance of around 3.6 Å and a density of 1.3 g/cm^3. We note that a second-shell distance close to 3.6 Å is what is derived for HDL by Soper and Ricci [14] in their study of water at different pressures and temperatures which suggests that the main-edge in liquid water is determined mainly by the local HDL-like component.

We can thus assume that both the pre-edge and main-edge spectral features depend both on the 2nd-shell distance and H-bond distortions. The proposed interpretation of the HDL in sect. **1** as a thermally excited version of high-density structures would lead to a combination of H-bond distortions in the first shell and the collapse of the 2nd shell. The H-bond distortions would naturally, through the expansion of the first shell, lead to a lower density than what is seen for the high-pressure ices. There is spectral information regarding the latter based on a close inspection of the energy position of the pre-edge

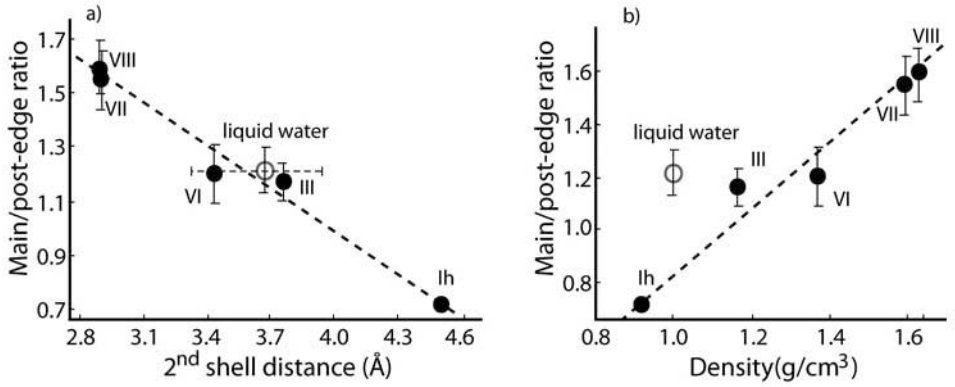

Fig. 11. – (a) Main-to-post-edge ratio as a function of the average second shell distance. (b) Density dependence of the main–to–post-edge ratio (adapted from ref. [96]).

peak. Figure 10b shows a closer view around the pre-edge spectral features for the ices and water at different temperatures. We note that the pre-edge shifts towards higher energy for the high-pressure ices in comparison to hexagonal ice. The reverse is seen for water where the pre-edge shifts to lower energy with increasing temperature, *i.e.* toward the gas phase $4a_1$ value [3,15]. Since the pre-edge feature is related to the distorted peak in the XES spectra, which also shifts towards the gas phase value, it is consistent that this shift reflects the H-bonding distortions in the first shell due to the thermal excitation of the HDL structure. We note that the pre-edge position of the high-pressure ices would not be discernible as a separate spectral feature in the liquid water spectrum since it would fall under the strong rise of the main edge.

It can be observed that there is also a shift to higher energy in the post-edge from hexagonal ice to Ice VI in fig. 10a. This is most likely due to a shortened H-bonding distance in the first shell. It has been observed that the post-edge obeys the principle of "bond length with a ruler" [97] for XAS [3,57,98]. This implies that the energy position of the post-edge should shift to higher energy as the H-bond becomes shorter since the post-edge is due to excitations into states that are antibonding with respect to the H-bond network and thus go up in energy as the distance is reduced. Finally, we note the very weak post-edge in Ice VII and near-absence of a post-edge in Ice VIII which is consistent with less directional H-bonding to minimize Pauli repulsion as the molecules are forced closer. Indeed, from vibrational spectroscopy the OH stretch frequency is observed to blue-shift for high-density ices [99].

3˙3. *Interpretation of XAS/XRS: Newns-Anderson model.* – Let us now generalize all the findings in a simple picture where we first artificially separate the electronic states on the excited molecule from the bath of electronic states in the surrounding condensed phase and then turn on the interaction between the two. The reason for this description is that the core hole potential will pull down the local atomic orbitals that build up the electronic structure of the core-excited molecule and this will change the electronic interactions with the surrounding condensed phase. We will in this simple picture consider the core-excited water molecule as a local impurity with a different set of molecular orbitals interacting with the surrounding bands of unoccupied character [17].

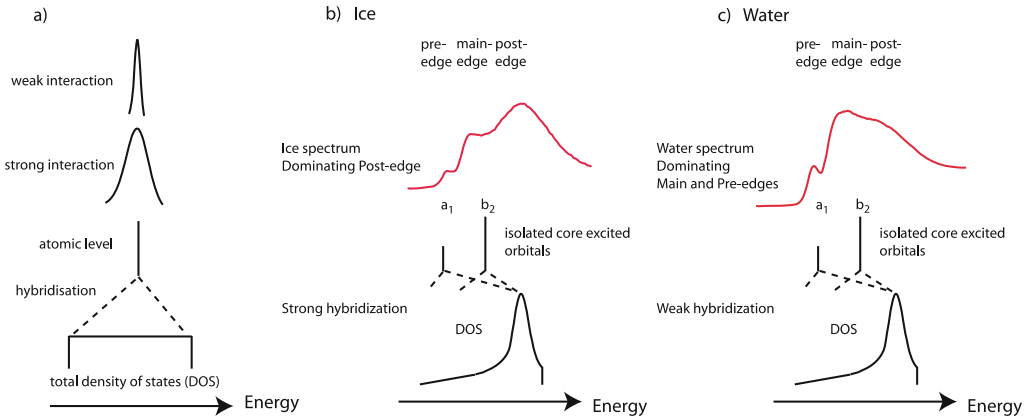

Fig. 12. – (a) Illustration of the Newns-Anderson impurity model [100,101] applied to an atomic energy level interacting with a broad featureless continuum of delocalized electronic states. The hybridization leads to a broadened resonance whose width depends on the strength of the interaction. (b) Schematic illustration of a simplified application of the Newns-Anderson impurity model to the XAS problem in ice where we have hybridization of the delocalized empty density of states (DOS) of the condensed phase with the isolated local molecular orbitals of the core-excited water molecule. The DOS of the condensed phase has a well-defined resonance that via strong hybridization with the core-excited molecule leads to the appearance of the post-edge. (c) The Newns-Anderson impurity model applied to water where the a_1 and b_2 core-excited molecular orbitals retain most of their isolated character but with different broadenings due to weaker hybridization with the water conduction band leading to the pre-edge and main-edge spectral features.

In order to facilitate this type of description we make use of the Anderson impurity model originally established to describe magnetic impurities in solids [100] and further developed by Newns for the case of adsorbed atoms interacting with a metallic substrate [101].

Figure 12a shows how a single atomic level of an atom interacts with a broad featureless continuum of electronic states resulting in a resonance that corresponds to a broadening of the level on the atomic site. The amount of broadening will depend on the strength of the interaction or, in another language, the degree of hybridization. For a completely featureless continuum interacting with a sharp atomic state the line shape of the resulting resonance can be expressed in terms of a Lorentzian with a specific width. If the continuum is not flat or the interaction is not equivalent with all parts of the continuum there will be distortions of the Lorentzian line profile. Furthermore, if there are sharp features in the continuum specific new resonances can be observed when measuring at the atomic site if the hybridization is strong; through the involvement of the core-hole X-ray spectroscopies give atom-specific information.

We next consider such a simple picture for the case of a core-excited water molecule interacting with the surrounding condensed phase as represented by hexagonal ice. There will be a downshift of the water molecular orbitals due to the core-hole potential where one screening $1s$ electron has been removed. We can understand such a shift if we consider the equivalent core potential where we replace the oxygen atom with fluorine ($Z + 1$ approximation). We regard the molecular orbitals of the excited molecule in terms of two resonances, a_1 and b_2 related to the gas phase spectrum as shown in fig. 12b and c. Theoretical calculations show that the unoccupied electronic density of states

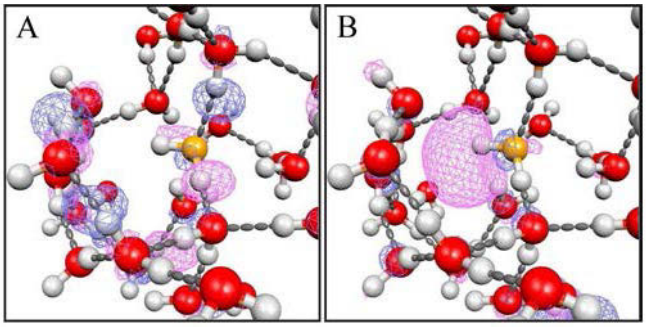

Fig. 13. – Orbital plots of core-excited states in (A) the post-edge region and the pre-edge region (B) with the core-hole on a single-donor species with the structure taken from a snapshot of an MD simulation [64].

(DOS) of ice has a well-defined strong resonance [102] which we denote the conduction band, but otherwise the DOS shows a rather featureless distribution which slopes in intensity towards lower energies. We should note that in the real system there will be a significant broadening of the strong resonance due to the large amplitude of the internal O-H zero-point vibrations in the water molecule [87, 103]. When we turn on the hybridization, the a_1 and b_2 levels will be broadened into resonances where the b_2 will interact more strongly since there is higher DOS at similar energies in comparison to the energy region close to a_1. However, most of the molecular character will still be visible in these resonances. The hybridization with the strong peak of the conduction band will lead to a new resonance that will mostly be of band structure character involving the surrounding molecules. We can view this as some admixing of the local $2p$ character on the core-excited molecule into the surrounding DOS. It is the local O $2p$ character that will provide most of the intensity in this resonance although it is fully delocalized into the whole condensed phase.

We can envisage the nature of the wave functions of the two most extreme cases, the pre-edge for molecules with a broken H-bond leading to a fully localized state on the free OH of the excited molecule and the post-edge where the water is fully H-bonded. The former has been shown to lead to a very localized state and the latter to a delocalized state where the residence time of the excited electron on the local molecule is less than 500 attoseconds using the core-hole clock method [64]. In fig. 13 we show plots of the wave functions of these two excited states. Indeed we observe that for pre-edge excitation the electron is clearly located only on the core-excited molecule whereas when the excitation is into the post-edge it is fully delocalized over many water molecules where the amplitude of the wave function follows the H-bonding network. The latter case shows how the delocalized nature of the surrounding band structure really determines the nature of the post-edge feature although it is measured only via the hybridization of the local O $2p$ character on the core-excited molecule.

Based on this simple picture we could ask ourselves how the spectrum will change as we modify the core-excited orbitals, the conduction band or the strength of the hybridization between the local states and the surrounding. Figure 12b represents the ice case when we have strong hybridization in the tetrahedral structure between the local core-excited orbitals and the DOS resulting in a strong post-edge. In the other extreme we have weak hybridization due to the collapsed 2nd shell and broken or weakened H-bonds in the first

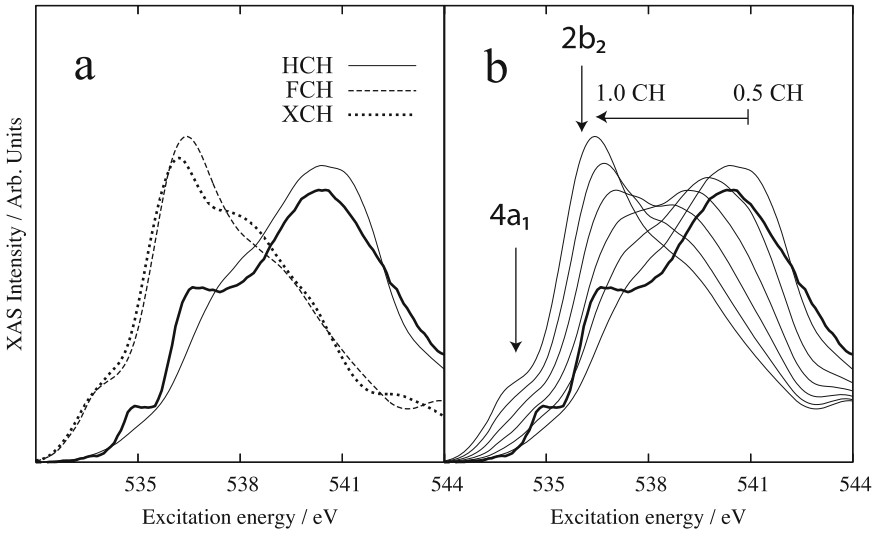

Fig. 14. – (a) Transition potential half-core-hole (HCH) (thin black line), full-core-hole (FCH) (dashed line) and XCH (including the screening excited electron) (dotted line) spectra computed from one bead of a 100 K PIMD ice simulation together with the experimental curve (thick black line) from ref. [85]. (b) The same summed spectrum computed with core-hole potentials spanning the whole range between a half- and full-core-hole, using respectively 0.50, 0.60, 0.70, 0.80, 0.90, and 1.00 core-hole. The arrows indicate the positions of the transitions in gas phase water. Figure from ref. [87].

shell in HDL resulting in a weak post-edge and instead strong features from the local core-excited orbitals. Here we assume that the weak post-edge in the water spectrum arises due to the specific tetrahedral LDL related structures.

We can demonstrate and confirm the qualitative picture from the Newns-Anderson model by calculating the spectrum of ice with different strengths of the core-hole potential by going stepwise from a half electron excited to the limiting case of a full electron being removed, see fig. 14b. Each spectrum in fig. 14 is the sum of 1326 spectra calculated for a single bead of a path integral MD (PIMD) simulation of SPC/E ice at 100 K where each spectrum is calculated using a cluster of 39 molecules extracted from the simulation [87]. Identically the same structures have been used in all the calculations with the only difference being the strength of the core-hole interaction with the unoccupied valence states. Note that an absolute energy scale is available such that all spectra have the same onset; it is only the intensity that becomes redistributed according to the strength of the interaction as indicated in fig. 12.

As the strength of the core-hole potential is increased the unoccupied states on the core-excited molecule are increasingly pulled down from the conduction band. As a consequence their interaction with the band states becomes weaker resulting in a spectrum resembling more and more that of the free molecule with features at energies corresponding more to those of the free molecule. This nicely confirms the qualitative picture from the Newns-Anderson model. In spectrum calculations where an absolute energy scale is not available, *i.e.* where pseudopotentials are used to eliminate the O 1*s* core levels, it is necessary to shift the spectrum to compare to experiment [58, 104, 105]. Figure 14a illustrates the difficulty in this approach when both spectrum shape and onset of intensity

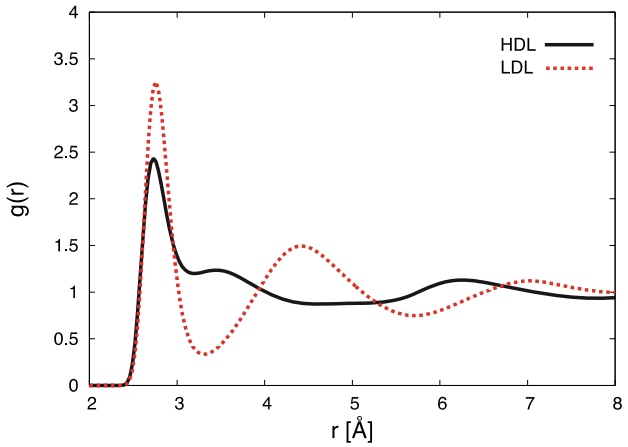

Fig. 15. – Comparison of experimentally derived LDL and HDL O-O pair-correlation functions from ref. [14].

depend strongly on how the core-hole is treated [56,106]. The half-core-hole (HCH) transition potential approach [107] gives the correct width and position of the ice spectrum, while the full-core-hole (FCH) [102] and core-hole with excited electron (XCH) [58] do not. Interestingly, the HCH spectrum is very similar to that of the monolayer of water presented in fig. 9, which may be the best experimental representation of completely H-bonded ice without structural defects; it is very difficult to create an experimental ice model free of defects [3] and it may even be the case that the energy deposited in the dominating Auger decay [108, 109] induces a local structure transition from tetrahedral to disordered when the environment is that of insulator ice rather than connected to a metal surface which can take up the released energy.

Improved approaches giving better agreement with experiment when computing XAS of water models have been developed based on the Bethe-Salpeter equation by Car and coworkers [102, 103] and Rehr and coworkers [110] but still suffer from not having access to an absolute energy scale and give less good agreement with the experimental ice spectrum in comparison to the HCH spectrum in fig. 14a. In this respect quantum chemistry based approaches are also of interest where complex polarization propagator techniques to compute XAS [111] have recently been extended to the CCSD level [112] giving promise of reliable calibration of different methods on reasonably sized water models.

4. – The inherent structure in MD simulations

Many molecular dynamics (MD) models that are used to describe water do indeed obtain HDL- and LDL-related structures in the supercooled regime (*e.g.*, [30,113-115]) but not at ambient conditions. In order to distinguish HDL- and LDL-like local environments in a simulation an order parameter that distinguishes the two is needed. Figure 15 shows the O-O pair-correlation functions for hypothesized HDL and LDL structures as derived from pressure-dependent neutron diffraction experiments [14]. HDL is characterized by the presence of interstitial molecules between the first and second hydration shells leading to perturbed hydrogen-bonding and higher density; this is seen as a collapse of the

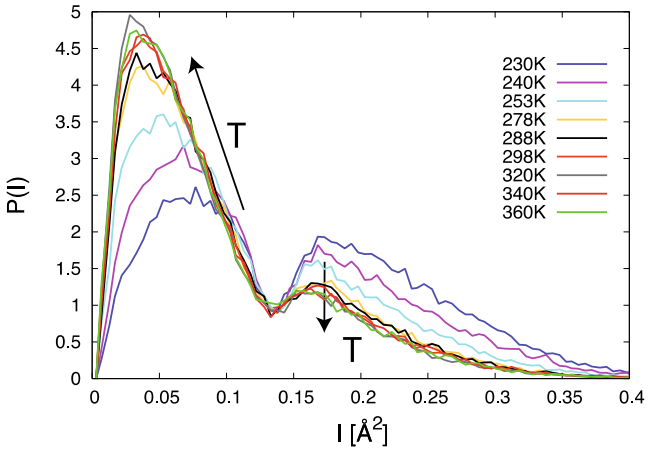

Fig. 16. – Distributions of the local structure index parameter $I(i)$ obtained from energy-minimized "inherent structures" in simulations at ambient pressure, shown as function of temperature. A temperature invariant isosbestic point is seen around $I = 0.13$–$0.14\,\text{Å}^2$. (Figure adapted from ref. [24].)

2nd-shell to around 3.5 Å as previously discussed with a shift to shorter distances also of the third shell. LDL exhibits more ice-like local order with well-separated first and second shells at 2.85 Å and 4.55 Å [14]. An order parameter that distinguishes HDL and LDL should thus take into account the structure out to the second shell. Here we use the local structure index, LSI, [116,117] which reflects the degree of order in the first and second coordination shells. In simulations of water, LSI gives a unimodal distribution peaking at low values (HDL-like) and extending to high values (LDL-like). When instead applied to the *inherent* structure in simulations of supercooled and ambient water a bimodal distribution of low and high values is found in support of an instantaneous two-state picture of water [24,118,119]; the inherent structure is obtained by quenching the instantaneous structure into the nearest local minimum on the underlying potential energy surface, thus removing effects of thermal excitations [120].

Here we apply [24] the LSI to the inherent structure in large-scale (45 000 molecules) molecular dynamics simulations [11] of TIP4P/2005 [121] water. In fig. 16 we show the evolution with temperature of the probability distribution of LSI values, $I(i)$, computed for inherent structures (IS) at 1 bar. A clearly bimodal character is observed at all temperatures. The same minimum is seen at various pressures as well [24]. The stability of the minimum at 0.13–$0.14\,\text{Å}^2$ at all temperatures and pressures is quite remarkable and a strong indication of a clear distinction between the two classes of local environments in the inherent structure. This implies that the $3N$-dimensional potential energy surface (PES) on which the simulation evolves contains two qualitatively different types of local projections relating to *local* configurations of molecules in agreement with the above-discussed XAS [3,18,40] and XES [23,122] experimental data.

There are sharp changes in the relative amplitude of the high-LSI and low-LSI peaks at deeply supercooled temperatures, while at higher temperatures the simulations sample very similar regions of the PES since only weak temperature-dependence is seen. A very clear connection to thermodynamic behavior is established in fig. 17 where we show the populations in each class as function of temperature using the minimum around $0.13\,\text{Å}^2$ as classification.

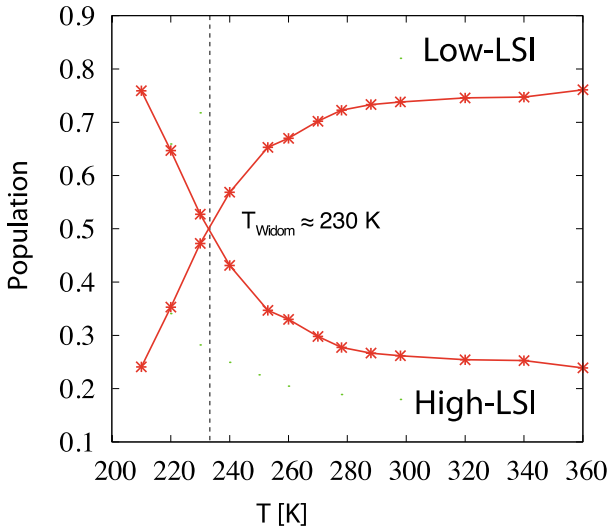

Fig. 17. – Temperature dependence of the relative populations of high-*LSI* and low-*LSI* species in the inherent structure of TIP4P/2005 water, defined according to the isosbestic minimum. The low-*LSI* and high-*LSI* curves are by definition mirror symmetric around population = 0.5. The temperature where a 1:1 ratio between low-*LSI* and high-*LSI* is realized coincides nearly perfectly with the Widom line of the model. (Figure adapted from ref. [24].)

In the LLCP scenario the two liquid phases, HDL and LDL, are assumed separated at elevated pressure and supercooled temperatures by a coexistence line terminating at a critical point where thermodynamic response functions diverge. In the one-phase region, thermodynamic response functions show maxima in the P-T plane defining the so-called Widom line as an extension of the coexistence line beyond the critical point [123]. The Widom line divides the one-phase region into regions dominated by properties characteristic of either phase, but the distinction, and magnitude of the maxima, diminish with increasing distance to the critical point [124]. Earlier studies [125] have located the LLCP and the Widom line of the TIP4P/2005 model where the LLCP was found close to $P_c = 1350\,\text{bar}$ and $T_c = 193\,\text{K}$ with the Widom line at $\sim 230\,\text{K}$ at 1 bar pressure. Figure 17 shows that the Widom line coincides closely with the temperature where a 1:1 ratio between low-LSI and high-LSI populations is seen [24,126], which is consistent with a maximum in fluctuations between the two and consequently in fluctuations of density, entropy and their cross-correlations.

Let us now relate the observed two populations of low-LSI and high-LSI species in the inherent structure of simulated water to experimental observations of real water. Figure 6a shows the temperature dependence in the lone-pair $1b_1$ region of the XES spectrum for D_2O [23]. We directly infer from the temperature dependence that the tetrahedral component is related to the high-LSI species and the distorted component to the low-LSI species. In particular we note from fig. 17 that the populations at ambient conditions, $\sim 25\%$ high-LSI (LDL-like) and 75% low-LSI (HDL-like), coincide closely to experimental estimates [15,23,127] of the two components in the XES and XAS/XRS [18,40]. Furthermore, the XES data also show quite weak temperature dependence in the ambient regime of the relative intensities of the two components, fully consistent with the temperature dependence of the two LSI components in fig. 17.

There is another important observation that can be made from fig. 16 in the ambient to hot regime where the peak position of the low-LSI component shifts to lower values with increasing temperature whereas the position of the maximum of the high-LSI component remains constant; the latter shifts first in the deeply supercooled regime. This has a direct correspondence in the XES spectra in fig. 6a, XRS in fig. 7a and OH stretch in fig. 7b where the tetrahedral peak remains at constant energy within the probed ambient temperature regime, which is fully consistent with the temperature dependence of the high-LSI component. On the other hand, the distorted component, which would correspond to low-LSI, continuously shifts, as previously shown, to higher emission energies, lower absorption energies and higher OH stretch frequencies towards the gas phase value indicating larger distortions and further weakened H-bonding similar to the shift to lower values of the low-LSI component with increasing temperature.

We thus have a direct correspondence between the two LSI components and the spectroscopic observations. However, this is only seen in the inherent structure in the simulation when the effects of thermal motion and disorder are eliminated. The simulation thus seems to contain the prerequisites for generating a bimodal spectroscopic signal in that the underlying potential energy surface on which the simulation evolves does contain two minima consistent with the interpretation of the spectra. However, seemingly the minima are too shallow such that, when a finite temperature is included, the simulation is not constrained by the minima and an average structure is obtained. In this picture the two minima would thus need to be deeper to constrain the simulation more closely to either minimum.

In simulations using classical force-fields there are several effects missing that could deepen the minima. One such effect is electronic structure cooperativity in H-bond formation which strengthens individual H-bonds if a more extended tetrahedral network is created [128,129]. This effect is included in *ab initio* MD simulations using density functional theory (DFT) and, indeed, the minimum corresponding to tetrahedral or LDL-like structures becomes strongly enhanced as exemplified by the melting temperature of ice simulated using the PBE or BLYP functionals, which is found to be around 420 K [130]. The balance has thus shifted strongly towards LDL. HDL is a more close-packed structure, where close-packing generally is given by more non-directional interactions. Non-local correlation, or van der Waals interactions, could thus enhance the other, HDL-like, minimum in the simulations. Indeed, including dispersion corrections to the BLYP functional lowers the melting point to 360 K [131]. For the liquid recent MD simulations using new functionals containing non-local correlation fully *ab initio* [19,132] find a dramatic structure change from a very LDL-like O-O pair-correlation function (PCF) with the PBE functional to a very HDL-like PCF with the vdW-DF2 non-local correlation functional [19]. The simulations in ref. [19] were however too small (64 molecules) and too short (10 ps) to reveal any fluctuations between HDL- and LDL-like configurations, should such be favorable, and were furthermore done at constant volume with the density set to the experimental at ambient conditions. Note, finally that quantum effects are also important where it has recently been found that strong H-bonds are further strengthened through more efficient delocalization along the H-bond while weak H-bonds are further weakened due to delocalization in the librational motion [133].

5. – Density fluctuations

The isothermal compressibility κ_T is a response function that is directly related to volume or density fluctuations. If we look at fig. 1 we see that for a typical normal liquid

κ_T decreases with decreasing temperature. This is quite expected since the amplitude of the thermal motion of the liquid decreases with decreasing temperature. It is therefore very surprising that for water this is true at high temperatures but then suddenly, when the temperature approaches the ambient regime, κ_T flattens out and then instead increases with decreasing temperature and seemingly diverges towards an inaccessible temperature of 228 K [7, 134].

In the supercooled regime this anomalous behavior is commonly viewed as due to fluctuations between HDL and LDL [4, 31] but no agreement has been reached as to whether the two types of liquid exist as single-phase in some part of the phase diagram. However, the anomalous behavior sets in already under ambient conditions where spectroscopic data using XAS/XRS and XES together with small-angle X-ray scattering (SAXS) indicate two specific local species in the liquid with instantaneous local patches of tetrahedral structures appearing that have a rather different density and that persist on some time-scale before collapsing back into the background normal-like liquid [15,127]; this picture thus extrapolates the behavior from deeply supercooled conditions into the ambient regime. The more open network of the tetrahedral structures generates local regions with lower density which results in the density maximum at 277 K (4 °C) as the density decrease due to fluctuations into LDL-like tetrahedral patches overcomes the increased density with cooling of the HDL-like background normal liquid (fig. 2); this is also the origin behind the change in sign of the thermal expansivity α_P in fig. 1c. When fluctuations open up to create the tetrahedral structures we have another contribution to κ_T that has the same sign as the thermally induced random fluctuations. However, the temperature dependence is the opposite. The anomalous contribution leads instead to an increase in the compressibility upon cooling since we expect that the patches of more compressible tetrahedral structures are formed with higher probability, can survive longer and grow in size when the temperature decreases and H-bonding becomes more important.

5˙1. *Normal and anomalous contributions to* κ_T. – There is no strict division based on thermodynamic grounds between normal and anomalous contributions to κ_T. However, both Conde *et al.* [135] and Kanno and Angell [8] have made such a division by observing the influence of small impurities of molecular compounds in water and then extrapolating to infinite dilution. The normal component follows an expected normal liquid behavior. Figure 18 shows the division of κ_T into two components for the two different extrapolations [8,135]. First we note that the normal component dominates at high temperatures and the anomalous component at low temperatures. The two contributions to κ_T become equal at 279 K (6 °C) and 273 K (0 °C) for the two decompositions. Note that, since HDL and LDL can be expected to differ strongly in their inherent compressibility, the fact that their contributions to the resulting κ_T are equal does not imply equal populations of the two types of local structures. However, it does demonstrate that there is an appreciable amount of anomalous contribution to the density fluctuations already in the ambient regime. It is therefore essential to realize that fluctuations into tetrahedral patches, or LDL-like local structures, are significant well above the supercooled region and contribute to water properties and dynamics in the otherwise HDL dominated liquid. We note that the XES, XAS/XRS and IR/Raman indeed show a decreasing tetrahedral component all the way up to the boiling point as discussed in sect. **2**. However, eventually the tetrahedral patches might become so small that the anomalous contribution becomes negligible. It has recently been proposed that this occurs just above the isothermal compressibility minimum [13].

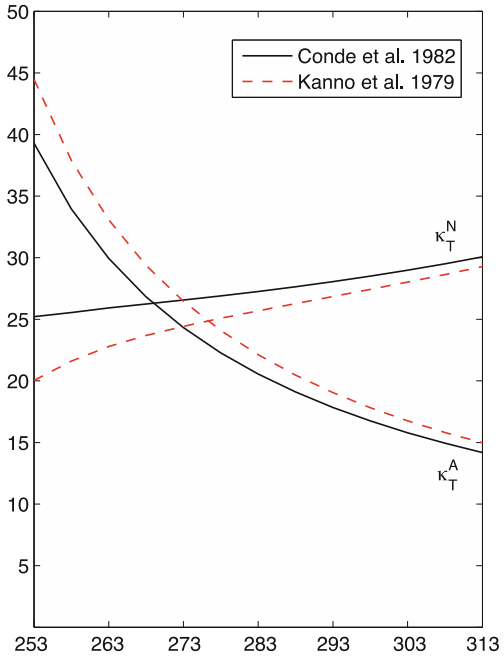

Fig. 18. – Normal and anomalous components of the isothermal compressibility of pure H_2O as obtained from Conde *et al.* [135] (full line) and as obtained by Kanno and Angell [8] (dashed line).

Based on fig. 1 we also note that the magnitude of the normal component is much smaller than what is expected for a normal liquid. However, what is interesting is that the normal component becomes quite similar to the full κ_T for water under pressure [135]. In this case the larger volume tetrahedral patches, or LDL structures, will be converted to the smaller volume HDL structures. Clearly the HDL structures are much less compressible than a normal liquid. This comes from the high density nature which we will return to later on.

5˙2. *Compressibility in MD models.* – In order for a water model to realistically describe both the structure and the dynamics of the fluctuations that occur in water at ambient conditions it is essential that such a large anomalous contribution to κ_T is well reproduced. Figure 19 shows computed κ_T from a number of MD models [136]. In the left part of the figure the TIP5P, TIP4P and SPC/E models are shown. First we note that all 3 models resemble more the normal liquid behavior in fig. 1 than real water, with a strong overestimation of κ_T at high temperatures and an underestimation at low temperatures. A real well-defined minimum in κ_T is also lacking in the studied temperature range. This means that there is only a negligible anomalous contribution to κ_T and instead the random thermal fluctuations clearly dominate. We should not expect to observe any major tetrahedral patches or local LDL structures to evolve in the ambient regime for these MD models, as was indeed not the case in the large-scale simulations of ref. [138]. We assume that a much larger anomalous contribution will appear deeper down into the supercooled regime since a LLCP with HDL and LDL local structures has been seen for these models [139]. This has indeed been shown to be the case for the TIP4P/2005 model where a significantly larger enhancement is seen at the Widom line

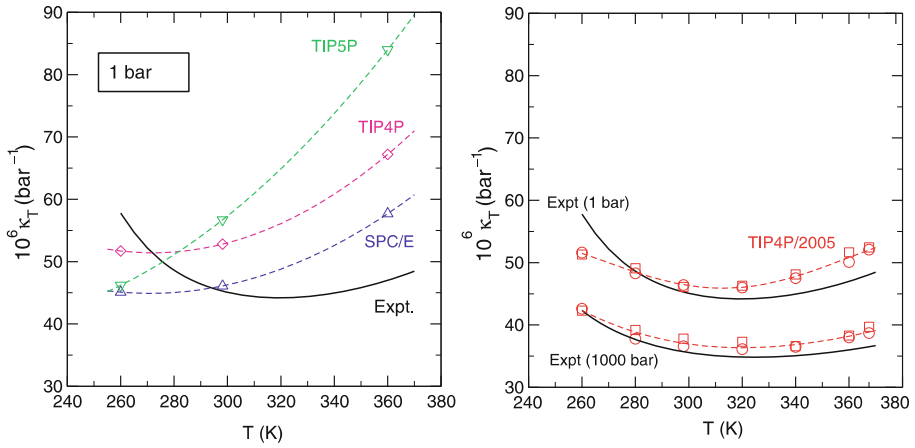

Fig. 19. – Isothermal compressibility obtained from molecular dynamics simulations [136] compared with experimental data [137]. Left: results for SPC/E, TIP4P and TIP5P at 1 bar pressure. Right: results for TIP4P/2005 at 1 and 1000 bar pressure.

(230 K) of the model [11], but, as is evident from fig. 19, at ambient pressure the model still severely underestimates structural fluctuations under supercooled conditions.

There is another important aspect that we can observe in a comparison between figs. 18 and 19 regarding the absolute value of the normal contribution to the experimental κ_T and the normal-liquid behavior of the MD models at high temperatures. The MD models are much more compressible than the normal component of the real κ_T. This means that, although the MD models behave more like a normal liquid, they are still far from a HDL-like liquid, which should have much lower compressibility. We can infer that in the MD models there must also be random fluctuations involving some sort of tetrahedrality which enhance the volume fluctuations. It seems that the MD models have stochastic fluctuations leading to a smeared out structure without generating spatially separated local regions of HDL and LDL structures. The amplitude of the stochastic fluctuations simply decreases with decreasing temperature. On the contrary the fluctuations in real water, that give rise to the anomalous contribution, are strongly correlated and lead to organized tetrahedral patches associated with larger volume and consequently lower density [15].

It is interesting to note that the SPC/E potential gives rise to a bimodal distribution in the inherent structure also in the ambient regime similar to what was presented in the previous section [118]. Clearly the thermal random motion smears this out giving only the normal liquid behavior of κ_T. We propose that the local potential energy minima related to HDL and LDL structures are not deep enough to give rise to the normal and anomalous parts of κ_T in the MD models. We would not expect to observe any major density inhomogeneities in the ambient regime for any of the models. We will discuss this further in the next section.

Before proceeding to discuss the structural implications of the anomalous contribution we should inspect the right part of fig. 19 that shows the temperature dependence of κ_T for the TIP4P/2005 model at two different pressures [136]. Here indeed we observe a minimum in κ_T that is not too far from the experiment. This is the reason why we have chosen to use this particular MD model for our simulations in the ambient and deeply

supercooled regimes [11, 22, 140]. However, in this context it is important to note that this model is not perfect. There is still an overestimation at high temperatures and an underestimation at lower temperatures although with respect to κ_T it is superior to the other models. It would be interesting to find an MD model that would underestimate κ_T at higher temperatures and overestimate at lower temperatures and investigate if in this case indeed local structures similar to what is observed in the inherent structure would also be seen in the real structure.

One such way would be to use the model at another thermodynamic state point to represent this aspect of ambient water. We note in fig. 19 that going to 1000 bar shifts the compressibility to lower values and that the simulation then is closer to the experiment at that pressure. This means that the model represents the fluctuations of HDL water with a low compressibility quite well. However, we note that the rise in κ_T at lower temperatures beyond the minimum is more rapid than for 1 bar. We could expect that the TIP4P/2005 model could have an even better representation of the balance between the normal and anomalous contributions to κ_T at 500–1000 bar higher pressure and 25–40 K lower temperature, which would be closer to the critical point in the model. This is also the case in terms of the phase diagram involving the various ices and liquid water for this model where such a shift would give a perfect agreement with the experiment [121].

Although we truly believe that the TIP4P/2005 model qualitatively captures both the anomalous and normal contributions to density fluctuations we know that the local nearest neighbor interaction is somewhat too strong. This gives rise to a too high and sharp first peak in the O-O pair-correlation function [61,62,121]. We can anticipate that this is part of the origin of the smearing of the two structures in the real structure. This will be further discussed below.

6. – Density inhomogeneities and Small-Angle X-ray Scattering

Let us now turn to the structural inhomogeneities that the anomalous part of the fluctuations give rise to. These have been interpreted as fluctuations involving local LDL patches that become more extended with decreasing temperature [15, 16, 141, 142]. In a more rigorous statistical-mechanical language these increased fluctuations into LDL patches have been called concentration fluctuations between different local structural environments [25] providing support for the interpretation of Huang *et al.* [15] in terms of density inhomogeneities due to fluctuations into tetrahedral patches, but using a different terminology.

6˙1. *Small-Angle X-ray Scattering (SAXS).* – Small angle X-ray scattering (SAXS) is the most direct probe of density variations or fluctuations on different length scales in a liquid. Through an enhancement of the structure factor in the region of low momentum transfer Q it can reliably identify small deviations from the average electron density due to instantaneous aggregation structures. Figure 20 depicts the scattering structure factor, $S(Q)$, at different temperatures varying from 347 K to 280 K [15] and from 284 K down to 252 K [21]. The experimental observation shows an enhanced scattering as Q approaches zero, indicating large density fluctuations in the system, which increase at low temperatures.

There is a thermodynamic relationship that relates κ_T to the structure factor at $Q = 0$ as $S(0) = k_B T n \kappa_T$, where k_B is the Boltzmann constant, T is the absolute temperature, and n is the molecular number density [143]. Figure 21 compares the isothermal compressibility determined from macroscopic thermodynamic measurements and as obtained

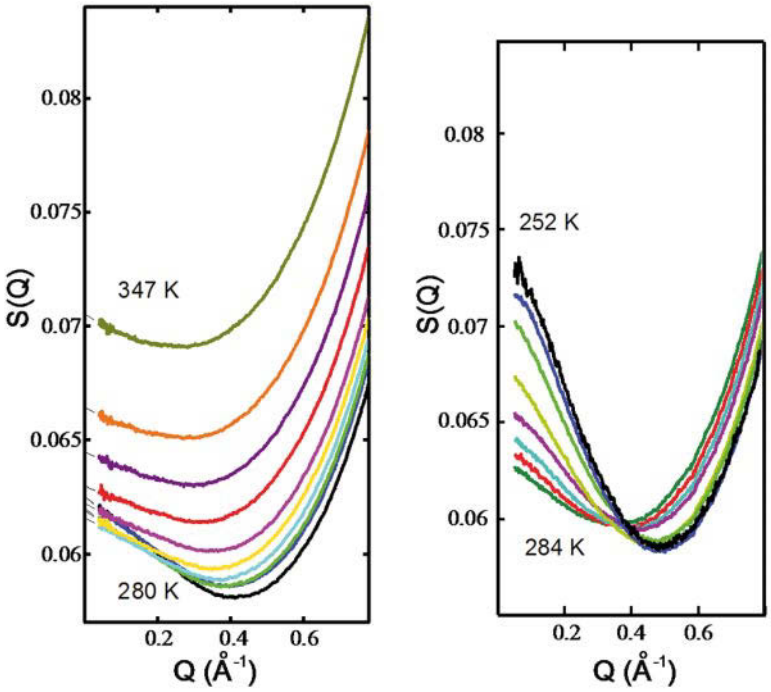

Fig. 20. – Experimental structure factor, $S(Q)$, derived from SAXS of H_2O, bottom to top at high Q: Left: 280, 284, 289, 293, 298, 302, 311, 320, 329 and 347 K [15] and (right, top to bottom at low Q) 252, 254, 258, 263, 268, 273, 278 and 284 K [21]. The extrapolations of scattering intensity to zero-scattering angle using a 2nd-order polynomial fit at low Q are represented by dashed lines in the left panel.

from the SAXS data [15,21] which demonstrates an excellent agreement. This shows that the anomaly of the minimum and then rise of κ_T towards cooler temperatures is directly related to the enhancement observed in the SAXS data and thus to the density inhomogeneity arising due to structural fluctuations [127]. Clearly this can be interpreted in terms of structural components due to the anomalous contribution to κ_T.

We now inspect the low-Q structure factor for a simple or normal liquid and how it varies with temperature. Figure 22a shows the temperature-dependent SAXS intensities of ethanol from 273 K to 328 K measured under similar conditions as in ref. [15]. First of all we observe no significant enhancement at low Q and secondly the shape of the curves is constant with only a vertical offset as function of temperature. This is clearly very different from the water scattering data in fig. 20 which show a similar offset at intermediate Q as ethanol with increasing temperature, but rather different behavior at low Q where the slope of the curve changes from positive to increasingly negative and with higher intercept with decreasing temperatures.

In fig. 22b we show the simulated temperature-dependent SAXS signal for SPC/E water using a simulation box containing 40000 molecules and sampled over 300–440 ps to reduce artificial oscillations. Due to the reciprocal correlation between r and Q space a large box size is needed to reach low Q; the mathematical properties of the Fourier transform from r space to Q space still prohibit observation of the behavior below $Q =$

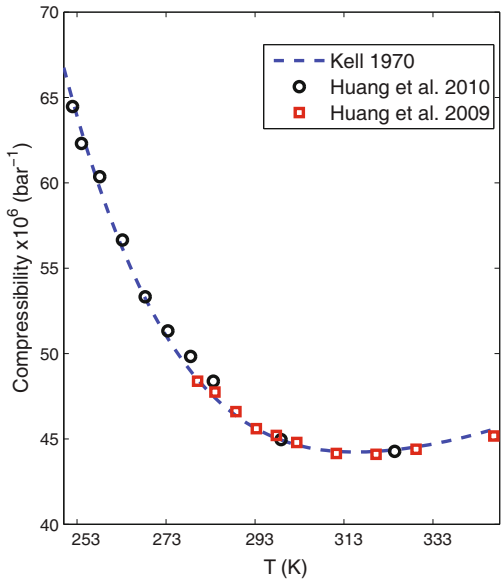

Fig. 21. – Isothermal compressibility determined from either macroscopic thermodynamic measurements (dashed line) [144] or extracted from the SAXS data (circles and squares) [15, 21].

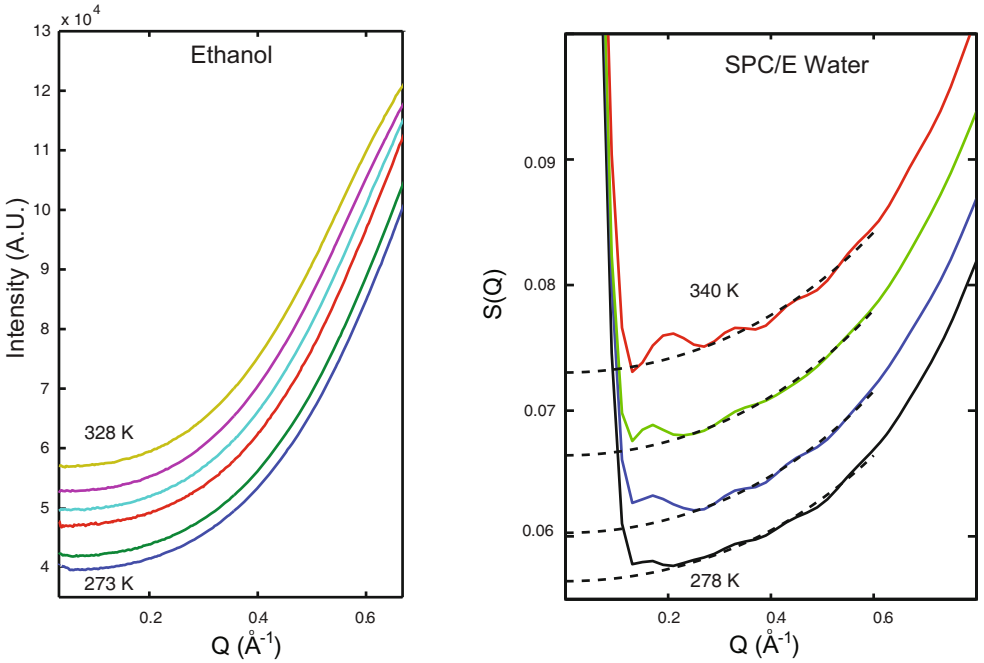

Fig. 22. – (a) Experimental SAXS intensities of liquid ethanol as a function of Q. The curves from bottom to top correspond to increasing temperatures of 273, 283, 298, 318 and 328 K. (b) Simulated curves for (bottom to top) 278, 298, 320 and 340 K SPC/E water [15]. The dashed lines indicate smooth curves where the anticipated effects of the box size and limited simulation time are removed.

$0.13\,\text{Å}^{-1}$ for the used box size $\sim 106\,\text{Å}$ (note that a weight function has been applied in the Fourier transform to reduce truncation errors beyond the reciprocal box size [11,15,145]). The most important scattering enhancement observed at small Q in the experiment on real water (fig. 20) is completely missing from the SPC/E water data even down to $Q = 0.13\,\text{Å}^{-1}$. The SPC/E simulated $S(Q)$ instead shows similarity with the experimental data for normal liquids such as ethanol (fig. 22a) and CCl_4 [15,17]. This is also what must be expected from the normal liquid behavior of SPC/E water in terms of the isothermal compressibility (see fig. 19).

6˙2. *Qualitative understanding of SAXS data.* – Let us now discuss what we would expect from a comparison between simulated and measured $S(Q)$ for different models. If a model, such as those shown in the left part of fig. 19, would be used we would not expect a rise in the low-Q region since the anomalous contribution to κ_T is too small. We can easily understand why there is no real enhancement at low Q, *i.e.* that there is no increase with a lowering of the temperature. The curves with positive slope at Q-values above $0.5\,\text{Å}^{-1}$ are related to the first diffraction peak in water, which, at higher temperatures, is broadened due to thermal disorder enhancing $S(Q)$ also at lower Q-values. The amplitude in the intermediate region before the first peak goes down with decreasing temperature simply because disorder is decreasing and the first peak gets sharper. This is seen for both the experimental and SPC/E simulated $S(Q)$. If we now look at the low-Q region we observe for the $S(Q)$ from the SPC/E simulation only a similar displacement with temperature as for the high-Q region causing the curves to become parallel. This is not surprising since we have the relationship between $S(Q)$ at $Q = 0$ and κ_T. If κ_T decreases with decreasing temperature it is expected that also the low-Q region will be lowered similar to the high-Q region.

However, for a model that indeed has a minimum in κ_T followed by a rise at lower temperatures we would expect the reverse. Now instead the low-Q region would increase upon cooling whereas the high-Q region would still decrease. This should give rise to a change of sign in $S(Q)$ to negative slope for low Q for models that have a large anomalous contribution. Maybe this is what we should expect for the TIP4P/2005 model, which fulfills this requirement.

Figure 23 shows the temperature-dependent $S(Q)$ for this model and indeed a change of sign is observed at low Q [11] for the 253 K simulation. This enhancement becomes much larger in the more deeply supercooled regime exhibiting a maximum between 240 and 230 K corresponding to crossing the Widom line in the model where the HDL:LDL ratio is close to 1:1 and the fluctuations show a maximum [11, 24] (see figs. 17 and 23 (right)). At even lower temperatures (220 and 210 K) the simulated liquid becomes increasingly dominated by LDL-like structures which reduces the structural fluctuations and as a consequence the low-Q enhancement. This demonstrates the connection between temperature dependence of κ_T and the enhancement at low Q. It is therefore clearly very important to develop water models that describe the anomalous or HDL-LDL fluctuations correctly.

This is further underlined by studying the isothermal compressibility of model water (TIP4P/2005 and SPC/E) down to deeply supercooled conditions and comparing with real water down to the lowest temperatures at which κ_T has been determined (fig. 24a); κ_T is related to $S(Q)$ at $Q = 0$ and can be extracted from, *e.g.*, the simulation in fig. 23 (left). In the present case the fluctuation formula was used instead which requires rather long simulations to converge. The simulations were thus run with 512 molecules for 1 microsecond for temperatures 230 K and lower and for the higher temperatures for 500

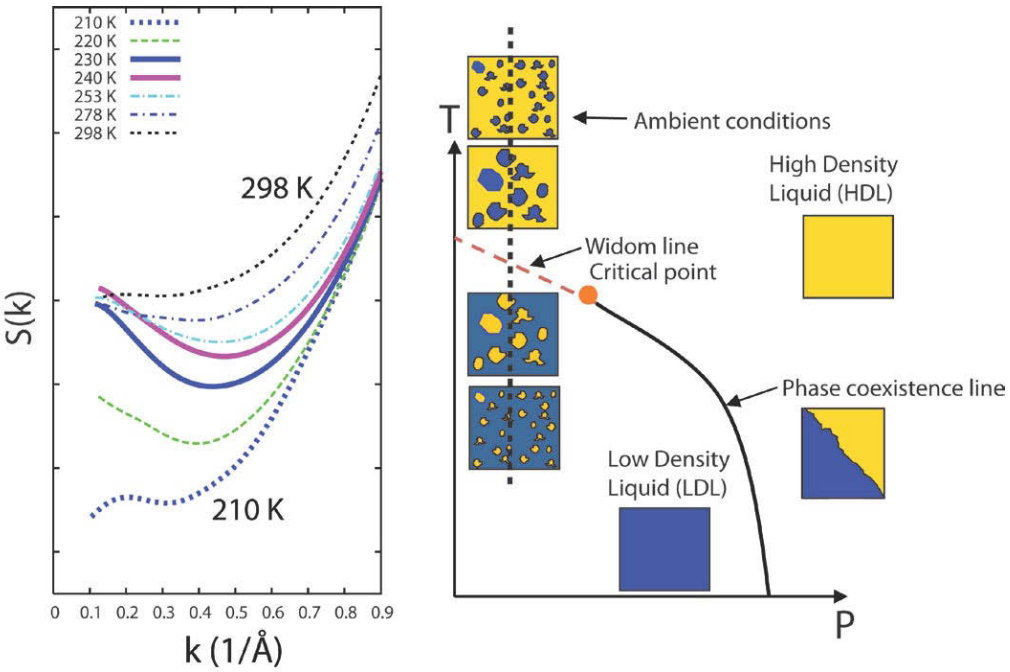

Fig. 23. – Left: The $S(Q)$ for (bottom to top at high Q) 210, 220, 230, 240, 253, 278 and 298 K TIP4P/2005 water using a simulation box containing 45000 molecules and run for up to 45 ns to reduce artificial oscillations [11]. The Widom line in the model lies between 230 K and 240 K (thicker lines) where the low-Q enhancement is maximal. Right: Illustration of the path (dotted vertical line) of the simulation (left) through a hypothetical phase diagram of real water to which the TIP4P/2005 model bears resemblance. At ambient conditions the liquid is dominated by entropy (HDL) with fluctuations into structures favored by enthalpy (LDL). Fluctuations increase when approaching the Widom line in the one-phase region beyond the hypothetical critical point. Beyond the Widom line collapse of tetrahedral structures into HDL like local structures occurs as fluctuations in the LDL dominated liquid, but fluctuations decrease further away from the Widom line which is also the case of the computed SAXS signal.

nanoseconds. We note for both TIP4P/2005 water and for SPC/E water a maximum in the isothermal compressibility as the Widom line in the respective model is crossed. We also note the significantly lower amplitude of the maximum for SPC/E water than for TIP4P/2005 water, which can be related to the distance to the liquid-liquid critical point in the respective models; fluctuations associated with a critical point decrease with increasing distance in the phase diagram from the critical point [124] and TIP4P/2005 water has its LLCP at $P_c = 1.35$ kbar and $T_c = 193$ K [125] while for SPC/E water an LLCP has been reported at $P_c = 2.90$ kbar and $T_c = 130$ K [147]. The significantly smaller rise for TIP4P/2005 water compared to real water then indicates that real water at ambient conditions should be significantly closer to its critical point than the TIP4P/2005 model. Indeed experimental and theoretical estimates of the location of the proposed LLCP of real water have placed it at a modest pressure of less than 500 bar [32, 148].

In fig. 24b we compare the computed SAXS signal from TIP4P/2005 water with the measured SAXS signal of real water. At the highest temperature shown (278 K) we note an excellent agreement between experiment and simulation, albeit with a small

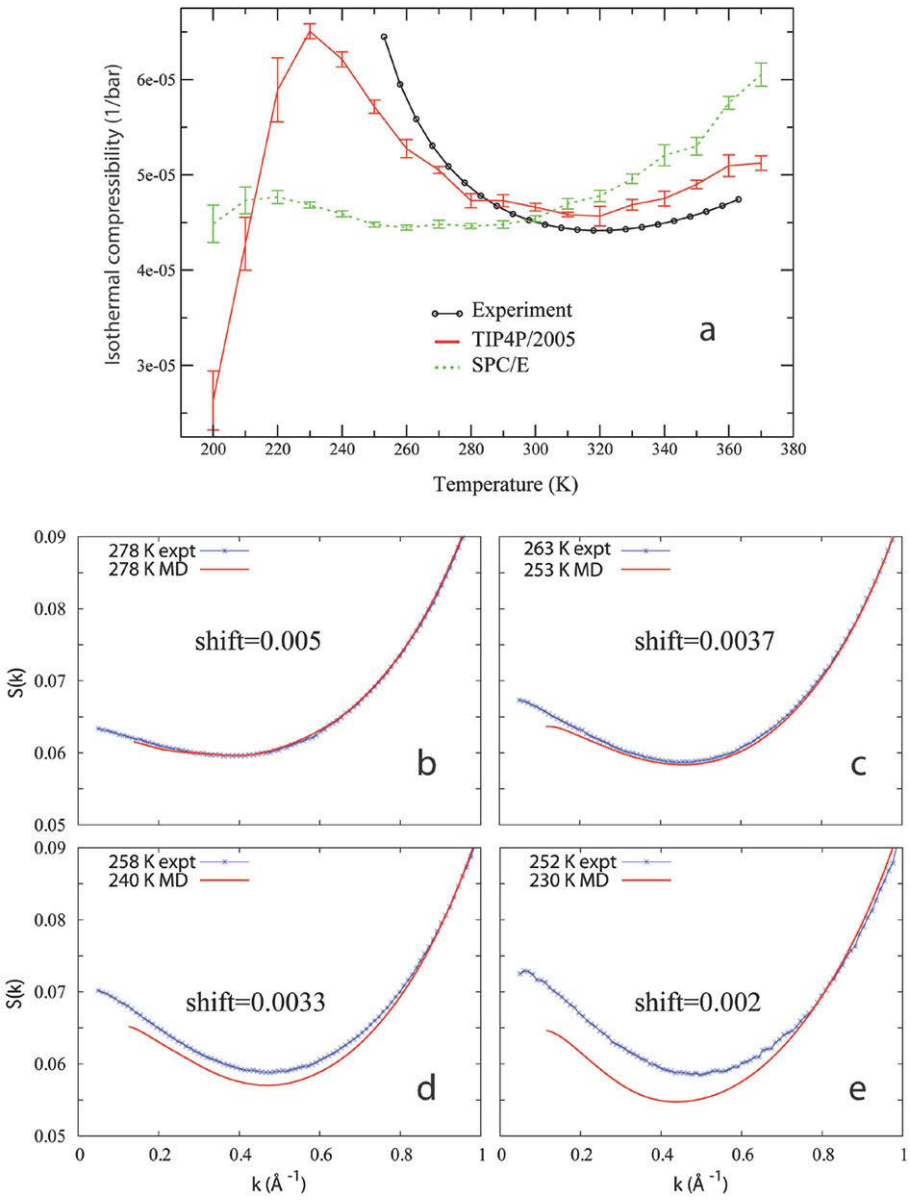

Fig. 24. – a) Temperature dependence of the isothermal compressibility for TIP4P/2005 water and SPC/E water compared with that of real water [146]. The compressibility of the water models was obtained from the fluctuation expression based on trajectories of length 1 microsecond ($T \leq 230\,\mathrm{K}$) or 500 ns ($T > 230\,\mathrm{K}$) with 512 molecules. b-e) Computed SAXS for TIP4P/2005 water compared to real water at temperatures (TIP4P/2005, real): b) (278 K, 278 K), c) (253 K, 263 K), d) (240 K, 258 K), e) (230 K, 252 K), *i.e.* an increasing off-set in temperature and absolute value for TIP4P/2005 water is required for best comparison with real water. At the Widom line (230 K) at ambient pressure for TIP4P/2005 water the SAXS signal is maximal but still underestimates the SAXS signal of real water at 252 K. Figure adapted from ref. [11].

shift of the simulated signal. However, going into the supercooled region we find it increasingly difficult to reproduce the experimental signal and an increasing offset, both in temperature and in magnitude is required for best fit to the experiment [11]. We note here that, even at the Widom line (230 K) of the TIP4P/2005 model where fluctuations reach a maximum, the anomalous enhancement is still smaller than experiment at 253 K [11] emphasizing that real water at ambient pressure is closer to a possible critical point, real or virtual, than is the case of the simulation.

6˙3. *The relation between correlation length and spatial extent.* – In order to obtain more information on spatial extent of fluctuations giving rise to the anomalous enhancement at low Q-transfer we consider Ornstein-Zernike (OZ) theory in which the total correlation, $h(r) = g(r) - 1$, between two particles is expressed as the sum of their direct correlation and the indirect correlations propagated via all other particles in the system [149, 150]; this is a widely applied framework for describing critical phenomena where the correlation length, ξ, tends towards infinity in the vicinity of a critical point, *i.e.* fluctuations become correlated at all length-scales. OZ theory is, however, quite general and can also be applied to, *e.g.*, describe the dynamical correlation between electrons in a molecule [151]; this is not at all related to critical phenomena, but simply a way to describe how one pairwise interaction can affect a second since that partner is part of another pair and so on *ad infinitum*. OZ theory simply describes in real space through the correlation length ξ how such indirect interactions decay.

In order to extract the correlation length from the data we fit the OZ expression for the structure factor, valid for small Q, $S(Q) \propto 1/(Q^2 + \xi^{-2})$, to the anomalous contribution to the structure factor [15, 17, 21]. The form of the function is a Lorentzian where the inverse correlation length, ξ^{-1}, is simply the half width at half maximum (HWHM). The extracted correlation lengths for supercooled water were obtained in ref. [21] and are shown in fig. 25 for different subtractions of the normal component. It is clear that the extracted correlation lengths are small, 2–3 Å, so how can this be understood and related to the real-space correlation? Is such a small correlation length, comparable to molecular dimensions, even relevant?

The Lorentzian above is the asymptotic expression valid for small Q and in order to relate to the real-space correlation function we must take the Fourier transform to obtain the asymptotic contribution to $h(r)$ [150], representing the main contribution for large r. This becomes $\exp(-r/\xi)/r$ showing that, in real space, the OZ correlation length simply has the role of a damping factor in the asymptotic decay of the total correlation. It is thus not a specific distance in the measured system and effects on the real-space correlation extend well beyond the OZ correlation length. To illustrate this point further we consider simulations close to the liquid-gas critical point (LGCP) of TIP4P/2005 water where the effects are significantly larger [11].

The simulations were performed in the NVT ensemble at the reported liquid-gas critical temperature and density [152] of the TIP4P/2005 force-field [121] using 45000 molecules in a box with ~ 163 Å sides [11]. The SAXS signal, $S(Q)$, was computed showing a very strong enhancement in magnitude at low Q due to the strong density contrast, but the extracted correlation length, or inverse HWHM, remained rather small, 5.9 Å, similar to earlier simulation results [153]. That this actually gives a good description of the asymptotic decay of the correlation function is seen in fig. 26 where we show the O-O $g(r)$ of the simulation near the LGCP together with the asymptotic function $1 + A\exp(-r/\xi)/r$ verifying that it describes the O-O $g(r)$ accurately beyond 6 Å (the factor $A = 1.4$ was fitted by hand) and that the enhancement clearly remains well be-

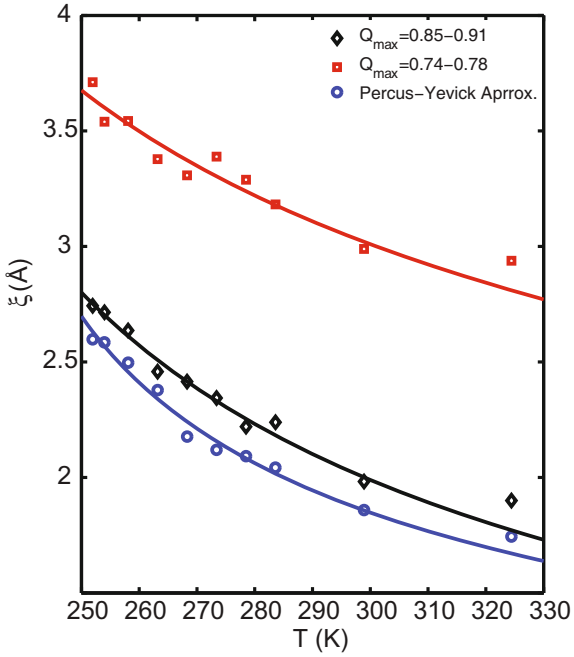

Fig. 25. – Dependence of correlation length ξ upon the temperature T for H_2O with a best-fit power law [21] with different subtraction of the normal component using either the Percus-Yevick approximation (circles) or the method used in ref. [15] with an assumption of the cut-off $Q_{\max} \approx 0.9\,\text{Å}^{-1}$ (diamonds) and $0.8\,\text{Å}^{-1}$ (squares).

yond 10 Å (the curve remains above the statistical mean of 1). Similarly OZ correlation lengths of $\sim$ 2–3 Å for ambient and supercooled water, as determined in refs. [15,21], will imply real-space correlations extending well beyond 2–3 Å.

To further illustrate the lack of a direct real-space correspondence between the correlation length and extent of actual spatial inhomogeneities in the simulation we show a snap-shot of the LGCP simulation in fig. 27 including a ruler showing the $\xi = 5.9$ Å correlation length as obtained from the simulation. In order to allow a visualization of the system we have cut a 10 Å thick slab from the $\sim$ 163 Å side simulation box. The granularity in the system is very visible and it is also clear that the granularity has a spatial extent which is significantly larger than the derived correlation length.

The same anomalous component in the SAXS data can, however, be analyzed in different ways depending on the expected character of the system. In terms of critical behavior the OZ fit is the established approach, but when dealing with, *e.g.*, macromolecules or colloids with fixed structure, the same curve shape would rather be analyzed in terms of a Guinier analysis [154] with the low-Q shape described by the scattering expression $\exp(-\frac{1}{3}R_G^2Q^2)$ with R_G the Guinier radius, which, in contrast to the OZ correlation length, in its interpretation is more directly related to real-space physical dimensions.

The X-ray photon interaction time with the probed electron density is of the order attoseconds, which implies that the SAXS experiment samples molecules frozen in time. It can thus be justified to consider analyzing the LGCP simulation in terms of a Guinier

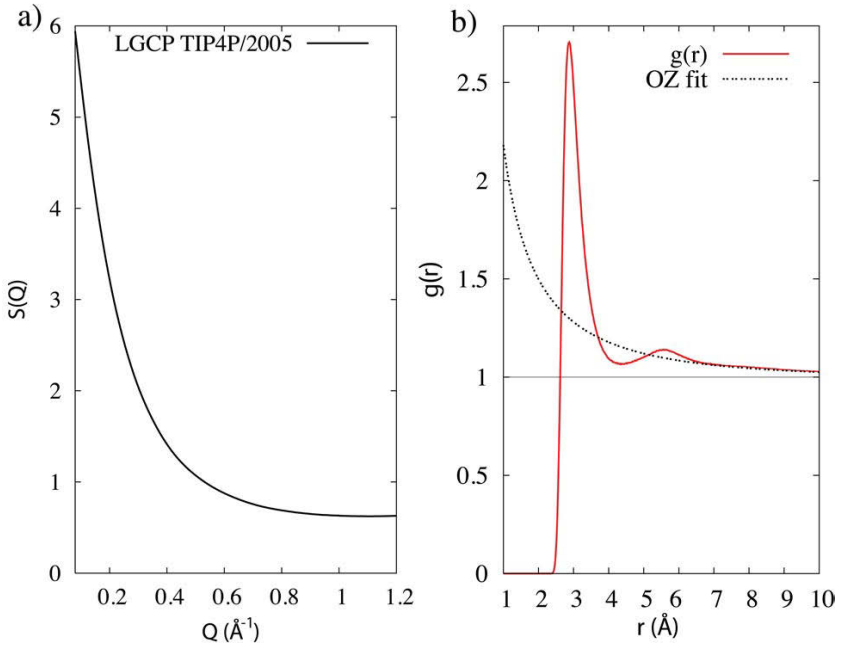

Fig. 26. – a) Small-angle structure factor $S(Q)$ from an NVT simulation at the reported liquid-gas critical point (LGCP: 640 K and $\rho = 310\,\mathrm{kg/m^3}$) [152] for the TIP4P/2005 model of water with 45000 molecules [11]. b) The obtained $g(r)$ together with the asymptotic OZ correlation function $1 + A\exp(-r/\xi)/r$ (dashed) which gives real-space correlations (in $g(r)$) even beyond 10 Å in spite of a correlation length ξ of 5.9 Å [11]. Reproduced with permission from Elsevier ref. [17].

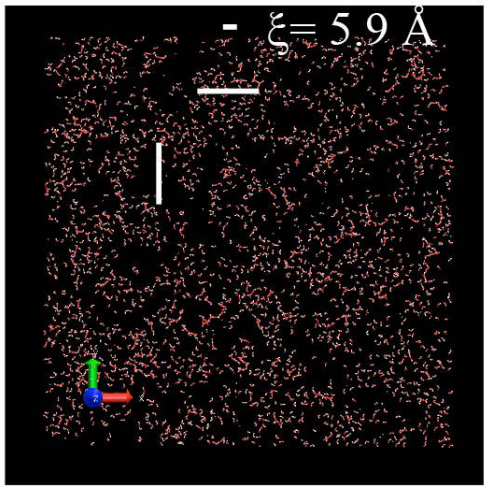

Fig. 27. – Snapshot from a TIP4P/2005 water simulation near the liquid-gas critical point including ruler showing the 5.9 Å correlation length on the same scale as the simulation box as well as measures (longer white lines) showing the Guinier estimate $D = 26$ Å of the spatial extent (see text).

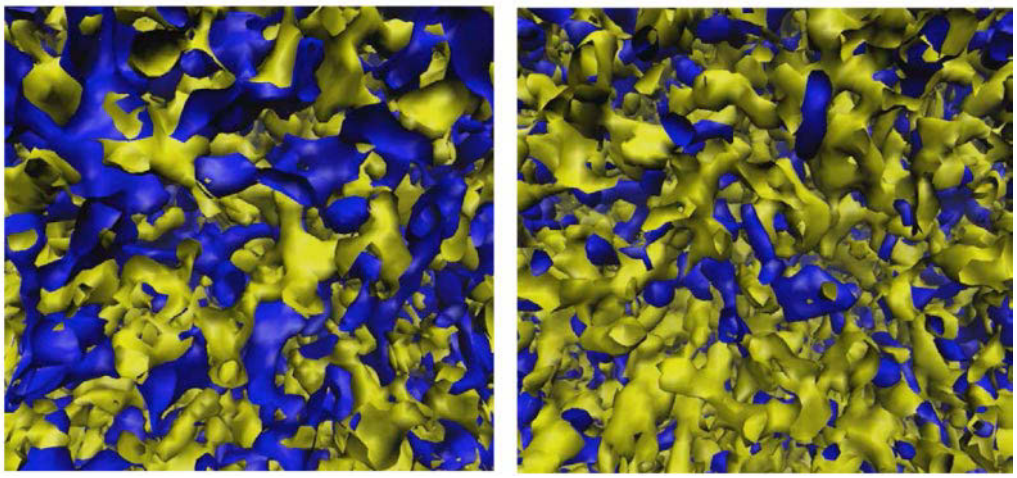

Fig. 28. – Isosurfaces at 253 K (left) and 340 K (right) of high-density fields (yellow) and high tetrahedrality (blue) from TIP4P/2005 simulations [11]. The length of the box is $\sim$ 106 Å. Reproduced from ref. [17].

analysis to obtain a better estimate of the real-space extent of the scattering density inhomogeneities. From the scattering expression one finds $R_G = \xi\sqrt{3}$ and, assuming a spherical shape, the diameter becomes $D = 2\sqrt{3/5}R_G$ which with $\xi = 5.9$ Å gives $D = 26$ Å. This is indicated in fig. 27 with the longer bars which clearly provide a better estimate of the actual size of the scattering inhomogeneities. However, we have to be aware that there will be many sizes, as is evident from fig. 27, and the derived value of D only gives a rough estimation of the mean value of the distribution.

6˙4. *Anticorrelation between tetrahedrality and density.* – Let us return to the TIP4P/2005 water model that indeed shows an anomalous behavior in the ambient regime both in κ_T and in the SAXS enhancement. Figure 28 shows colored regions in a simulation box at 253 K and 340 K of TIP4P/2005 water where two different selection criteria have been used of either high tetrahedrality (blue) corresponding to LDL or high density (yellow) as HDL and indeed we observe a spatial separation [11]. We clearly see the inhomogeneous structure where the regions of LDL and HDL occupy different parts in the real space. It is also remarkable to see that the inhomogeneous structure is maintained even at the high temperature of 340 K although the tetrahedral regions have become smaller. It should be noted here that high tetrahedrality and high density are strongly anticorrelated [11] such that the pictured inhomogeneity is not the result of clipping a single Gaussian field [155] although it is clear that varying the thresholds for tetrahedrality respectively density affects the appearance of a single snapshot. However, the comparison between snapshots at different temperatures using fixed thresholds is not affected by the specific choice of threshold (fig. 28). We have also observed that low- and high-LSI species, as defined in the inherent structure, form regions in the real structure [24]; here the strict bimodality given by the LSI index in the inherent structure gives an unambiguous decomposition. Although the strict bimodality in local structure is washed out by the thermal motion the clustering together is maintained.

7. – Wide-angle scattering and pair-correlation functions $g_{OO}(r)$

The O-O, O-H and H-H pair-correlation functions (PCF) provide a much used test of the performance of models of water in MD simulations in terms of structure. It should be noted, however, that X-ray and neutron diffraction are rather insensitive to H-bonding and caution must be exercised when drawing conclusions on the reliability of MD simulation results based on diffraction data; reproducing the experimental structure factor or the PCF:s is a necessary but not sufficient validation of the structure model from the simulation. Note that, when fitting structure models to diffraction data, a rather broad range of models in terms of H-bonding and O-O-O angular correlations reproduce the data [61,62,156]. Indeed, using reverse Monte Carlo (RMC) to model diffraction data and investigating the sensitivity of the combined X-ray and neutron diffraction data to H-bonding by either minimizing or maximizing the number of H-bonds in the fit resulted in equally good fits for models in the range of 20:80 to 80:20 in terms of asymmetric single-donor species *versus* tetrahedral double-donors [62]. With these caveats it is still a necessary requirement that a water model reproduces the experimental structure factor $S(Q)$ and the derived PCFs.

A difficulty for simulators has been to select which PCF to compare to, where in particular the range of published O-O PCF's has been problematic. In order to remedy this situation we have measured temperature-dependent X-ray diffraction of water with a unique set-up where we experimentally separate the elastic contribution from the Compton scattering using an X-ray spectrometer [22]. The water sample was a liquid jet eliminating contributions from a container and the water flow also minimizes any potential beam damage effects. A higher Q-range furthermore allowed us to obtain more details in the pair-correlation function and their dependence on temperature. Finally, we have recently published a detailed analysis of this and three other recent data sets going up to high Q-transfer and derived a converged benchmark O-O PCF [157]. In the following we will discuss different aspects of the O-O PCF starting with intermediate range correlations.

7˙1. *Correlations at intermediate range* (6–15 Å). – An issue of debate is the interpretation of SAXS data in terms of density heterogeneities and their size [11, 15, 16, 24, 29, 127, 138, 158, 159] where MD simulations have been shown to result in the expected unimodal Gaussian density distribution. However, it has also been shown that the LSI index determined in the inherent structure of TIP4P/2005 water divides the distribution into a sum of two superposed, shifted Gaussian distributions which behave with temperature similar to what is expected for HDL respectively LDL-like components [24]. In sect. **6** above we discussed the correlation length and how it is connected to the real structure only through the asymptotic decay of the pair-correlation function. We showed that the Guinier analysis gives a better estimate of the size of density fluctuations in water simulated close to the liquid-gas critical point of TIP4P/2005 water. This provides support for using the Guinier analysis also for experimental SAXS curves of *ambient* water which has led to an estimated average size of density heterogeneities ~ 1 nm [15], still assuming fluctuations between distributions of structures, but on a time-scale significantly longer than the attosecond experimental probe. We have recently confirmed the 1 nm characteristic average length scale by considering the O-O pair-correlation function at longer distances. Here we focus on the correlations at longer distances that are relevant in connection to the discussion of the SAXS data.

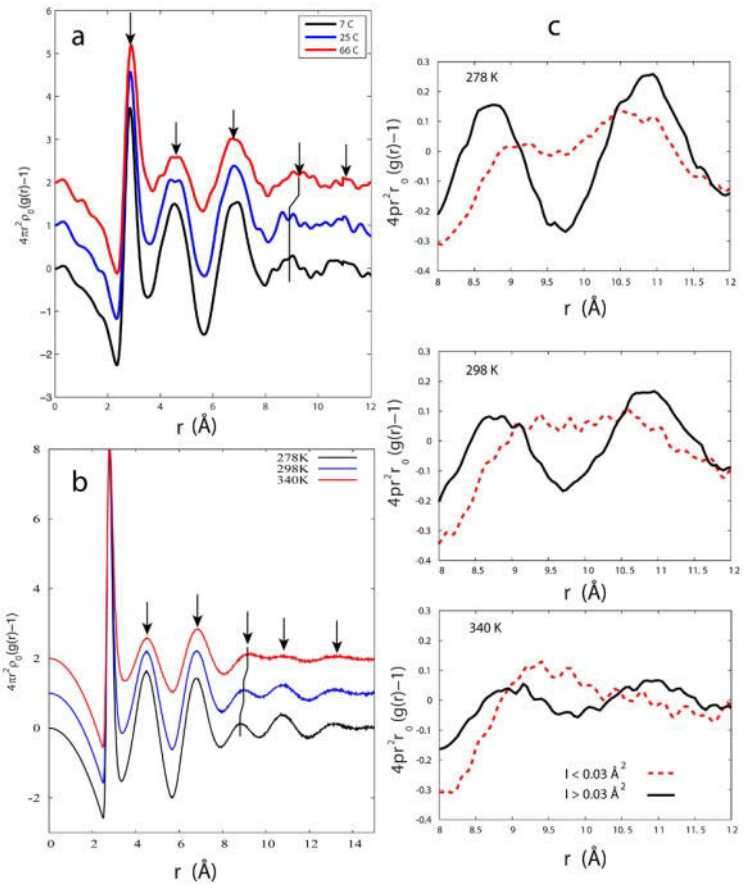

Fig. 29. – Comparison of the dRDFs derived from (a) XRD measurements from ref. [22], (b) a MD simulation using the TIP4P/2005 force field, and (c) focusing on the intermediate range (8–12 Å) in the simulation with separate contributions from molecules with LSI index above and below 0.03. From top to bottom 278, 298 and 340 K. For clarity, the dRDFs (defined on the vertical axes) are shifted vertically in (a) and (b); temperature decreases from top to bottom as labeled. The locations of the five structure peaks resolved from the experiment are marked by arrows in (a). Dashed lines are drawn to indicate the shift of the 4th peak in both experiment and simulation. In order to reduce the truncation oscillations in the large-r range, a larger damping factor of $\alpha = 0.018$ is used in the Fourier transform of experimental data. Figure adapted from ref. [22].

The pair-correlation function (PCF) at intermediate distances is magnified by plotting in fig. 29a the scaled difference in the radial distribution function (dRDF) defined as $4\pi r^2\rho_0(g(r)-1)$ [22]. We observe structural correlations up to $r \sim 12$ Å, indicating the presence of a medium-range order in the liquid. In particular, the 4th PCF peak at $r \sim 9$ Å and the 5th peak at $r \sim 11$ Å are resolved while after the 5th shell, the correlations are gradually washed out within the noise level of the experiment. A 5th PCF peak, similar to the present data, has been observed in supercooled water in two previous independent X-ray studies [160,161]. Yokoyama *et al.* [160] studied both supercooled and ambient water,

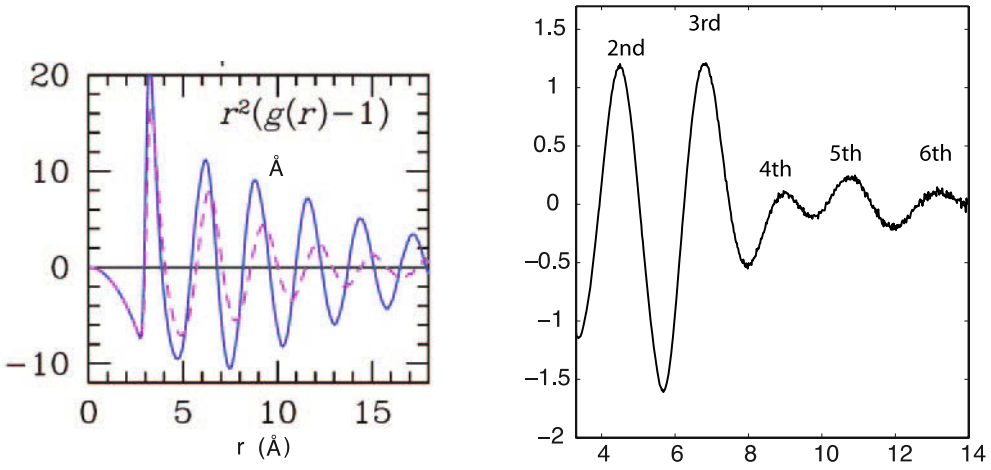

Fig. 30. – a) O-O dRDF for a Lennard-Jones (LJ) liquid for two reduced densities from fig. 1 in ref. [164]. b) Intermediate range correlations in the benchmark O-O g(r) from the APS data set with $Q_{\max} = 26\,\text{Å}^{-1}$ showing six well-resolved shells going out to $r \approx 14\,\text{Å}$ [157].

but the signal-to-noise level made it difficult to draw firm conclusions on intermediate-range correlations at 25 °C. However, in a very recent X-ray diffraction study of ambient water using 115 keV photons giving high-quality data out to $26\,\text{Å}^{-1}$ [162, 163] also a 6th coordination shell (fig. 30b) was observed at $\sim 13\,\text{Å}$ in ambient water [157].

7˙2. *Temperature dependence of intermediate-range correlations.* – There are interesting differences in the temperature dependence of the different O-O PCF peaks as shown in fig. 29a: the 1st and 4th peaks exhibit less temperature sensitivity compared to the 2nd, 3rd and 5th peaks whose magnitudes strongly increase as temperature decreases from 340 K to 280 K. It directly indicates that there are temperature-dependent structural changes in liquid water in addition to the effects of disorder induced by normal thermal motion.

In order to extract further information we compare to the dRDF from the TIP4P/2005 model as shown in fig. 29b. The simulation clearly contains the experimentally observed intermediate-range correlations giving the 4th and 5th PCF peaks in the correct positions. In terms of the temperature dependence, an excellent agreement between the MD simulation and experimental data is found: the 5th peak at $r \sim 11\,\text{Å}$ is observed to significantly increase in amplitude with decreasing temperature both in the XRD data and in the TIP4P/2005 simulation while the amplitude of the 4th peak exhibits less dependence on temperature. Moreover, the position of the 4th peak is seen to shift to larger distances at higher temperatures as indicated by the vertical line in fig. 29b; this is consistent with the shift observed between 280 and 340 K in the experimental data shown in fig. 29a.

To investigate the structural origin of these peaks at intermediate distances we characterize the molecules in the simulation according to the LSI parameter (discussed in sect. **4**), $I(i)$, and thus define sub-ensembles of water molecules in either disordered or structured environments. Since at the highest temperature, 340 K, rather few molecules are LDL-like according to the strict bimodal criterion of an $I(i)$ value greater than 0.13–

$0.14\,\text{Å}^2$ in the inherent structure we will here make a more qualitative division which gives an approximately 50:50 distribution at the lowest temperature 280 K; in terms of the associated PCF there is a continuous transition between HDL- and LDL-like when going from low to high $I(i)$ which implies that a lower cutoff will give the same qualitative trends, albeit less extreme. We thus use a cut-off $I_c = 0.03\,\text{Å}^2$, which gives relative populations of high-LSI species of 49%, 44% and 38% at 278 K, 298 K and 340 K, respectively, in order to follow the qualitative trends. Figure 29c shows the decomposed O-O dRDFs in the region of the 4th and 5th hydration shells, where each component reflects the environment around the respective species (*i.e.* including both intra- and inter-species correlations). Note that the decomposed dRDFs have been scaled by the relative fractions of low-LSI or high-LSI species.

We observe that high-LSI species (LDL-like) display two well-defined peaks around 8.7 and 11.0 Å, close to where the 4th and 5th peaks are observed experimentally as shown in fig. 29a. Both peaks decrease rapidly in amplitude at higher temperatures, in part due to the decreasing population of high-LSI species. On the other hand, low-LSI species (HDL-like) exhibit a very different behavior where a rather broad plateau centered around 9.5 Å at 298 K gradually develops into a peak at the *highest* temperature, 340 K. This unusual temperature dependence is responsible for the shift of the 4th PCF peak to larger distances at higher temperatures and the weaker temperature dependence of its amplitude compared to that of the 5th peak as observed in fig. 29b; the gain in intensity of the low-LSI species with increasing temperature in the region of the 4th peak compensates the loss of contributions from high-LSI species explaining the apparent weak temperature dependence of this peak while, in contrast, both the 3rd and 5th peaks lose amplitude with increasing temperature.

The close similarity between simulated and experimental intermolecular PCFs on the intermediate length scale suggests that the 4th and 5th correlation peaks, and in particular the latter, are attributable to the existence of fluctuations into highly ordered (LDL-like) structural environments in ambient water. The loss of intensity in the 5th peak with increasing temperature can then be regarded as a sign of conversion of LDL-like to HDL-like species upon heating alongside the increased thermal disorder, as reflected also in simulations by the diminishing contribution from high-LSI species at higher temperatures seen in fig. 29c. That we observe correlations of local LDL structures out to 11 Å [22] or even 13 Å [157] (fig. 30b) fully supports the interpretation of the SAXS data in terms of fluctuations on some time-scale resulting in local patches of tetrahedrally H-bonded molecules with characteristic size around 1 nm [15, 127].

It is interesting to compare the observed medium-range order in water with that of a simple liquid. For example, a Lennard-Jones (LJ) liquid also exhibits long-range ordered structure, as shown in fig. 30a, solely governed by the effect of packing in the liquid. The fundamental difference between the dRDF functions of the LJ liquid and water, however, lies in the fact that the correlation peaks in dRDF decay smoothly in the case of the LJ liquid (fig. 30a) while water shows a nonmonotonically decaying envelope function that is strongly r-dependent and where furthermore the peaks exhibit a more complicated dependence on temperature (fig. 29a, 30b). It implies that a single packing structure, such as for the LJ liquid, is not enough to explain the structure of liquid water. Using a simplified core-softened model, Perera explained the abrupt drop of the amplitude of the correlation peaks in the dRDF beyond the 3rd coordination shell as a consequence of destructive cooperation between H-bonding and packing correlations at large distances [164]. This is fully consistent with respect to the proposed regions of HDL and LDL local structures.

7˙3. *The first O-O peak.* – Even though TIP4P/2005 water reproduces the peaks at intermediate range in the O-O PCF together with their temperature dependence the first peak is significantly too high and sharp with a height above 3 [121]. In comparison with the PCFs derived in 2000 by Hura *et al.* [165] based on an X-ray diffraction data set going out to only $10.8\,\text{Å}^{-1}$ and by Soper [166] based on an EPSR analysis of neutron diffraction data, the peak height was too high, but the discrepancy was not too alarming. However, both these PCFs show a significantly too high first O-O correlation, but for different reasons. Due to the small Q-range measured by Hura *et al.* a Fourier transform of $S(Q)$ to real space could not be performed and instead the data in terms of the total scattering $I(Q)$ was fitted based mainly on PCFs from MD simulations under the assumption that the MD PCFs provided a sufficient range of possible PCFs. However, the total $I(Q)$ is dominated by the molecular structure factor masking the weaker intermolecular scattering such that small, but significant, deviations were not taken into account [62]. Similarly, the EPSR fit applied by Soper uses an initial MD force-field which is modified iteratively to give structures that reproduce the experimental scattering data. However, neutrons are more sensitive to O-H and H-H correlations than to the O-O correlation such that the initial overstructuring in the first O-O peak from the MD force-field was not fully corrected by the data. Since the two investigations, using very different techniques and appearing closely in time, arrived at similar results for the first O-O peak this was taken as evidence of a correctly derived O-O PCF and this was for long the standard comparison for developers of MD force-fields.

However, when actually fitting the Hura *et al.* data set using either RMC [61, 62] or EPSR [167] together with neutron diffraction data with large Q-range the peak height came down to a low 2.3. This then initiated efforts to establish experimentally with low uncertainty the shape and position of the first peak by extending measurements to higher $Q_{\max}$ with improved statistical accuracy [22, 162, 163, 168, 169] resulting in an experimentally agreed upon benchmark O-O PCF [157]. The new benchmark O-O PCF gives a peak height of 2.57(5) at a distance of 2.80(1) Å; the O-O PCF derived by Soper based on the same data is fully consistent with this analysis [170]. The PCF is given in numerical form in the supplementary material accompanying ref. [157].

For the data set going to highest Q ($26\,\text{Å}^{-1}$) [162, 163] a series of Fourier transforms were performed truncating the data at the different zeros in the structure factor which was used to establish the minimum $Q_{\max}$ necessary for a converged O-O PCF (fig. 31) with respect to the Fourier transform of the structure factor [157]. It is clear that a high $Q_{\max}$, greater than $18\,\text{Å}^{-1}$, is necessary to converge the first peak in terms of position, height and shape; lower $Q_{\max}$ values lead to a lower height of the first peak. Indeed, when fitting the Hura *et al.* [165] data with $Q_{\max}$ $10.8\,\text{Å}^{-1}$ using either empirical potential structure refinement (EPSR) [167] or RMC [61,62] a low peak height of 2.3 was obtained in agreement with fig. 31b, but in contrast to the original analysis where a peak height of 2.8 was estimated. Note that also O-H correlations contribute to the X-ray scattering and must be removed to derive the O-O correlation from Fourier transformed experimental data as discussed in ref. [157]; in RMC and EPSR fitting this is taken into account as part of the procedure.

8. – The HDL local structure

What is the nature of the H-bond distorted HDL structure that dominates at ambient pressures and temperatures? The driving force to energetically allow for the formation of HDL must be the more isotropic van der Waals interactions [19] together with quantum

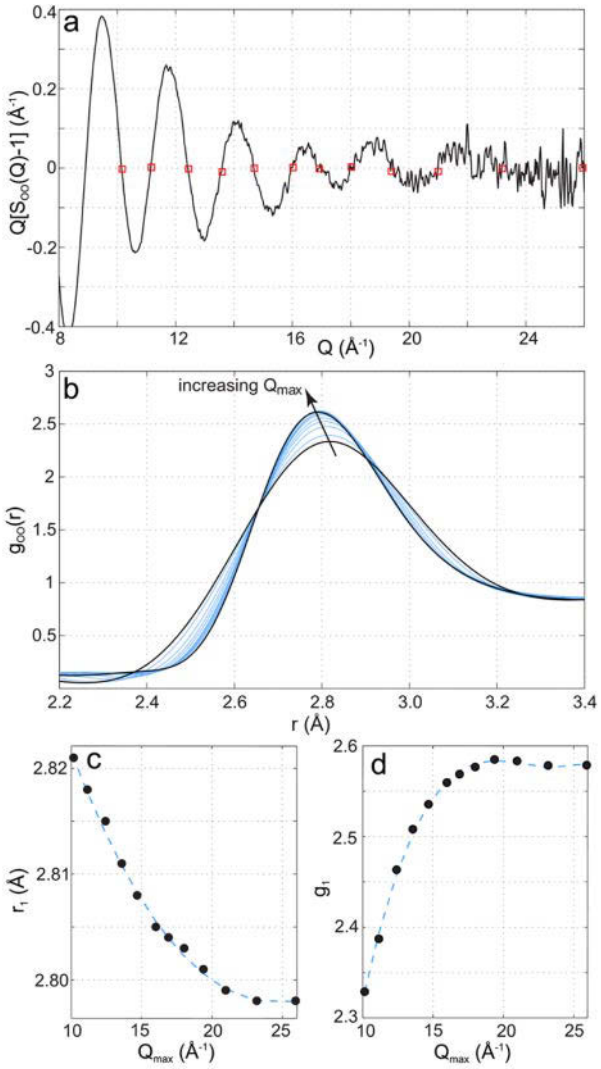

Fig. 31. – Demonstration of the effect of a limited maximum Q-value ($Q_{\max}$) in the Fourier transform of $S_{\mathrm{OO}}(Q)$, using the *APS* dataset. (a) The $S_{\mathrm{OO}}(Q)$ data is truncated at $S_{\mathrm{OO}}(Q) = 0$ nodes indicated by the red squares. The first-neighbor region of the corresponding $g_{\mathrm{OO}}(r)$ functions is shown in (b). The arrow indicates the trend with increasing $Q_{\max}$. The position of the first O-O peak maximum (r_1), and the peak height (g_1) are plotted as a function of $Q_{\max}$ in (c) and (d), respectively. Both peak position, r_1, and height, g_1, are found to be sensitive to the value of $Q_{\max}$ for values smaller than $20\,\text{Å}^{-1}$. Reproduced from ref. [157].

effects leading to strengthening strong and weakening weak H-bonds [133, 171] and, in addition, to quantized librational modes which become thermally inaccessible in tetrahedral coordination and thus do not contribute to the entropy. Tetrahedral ice is quite unique among all the condensed structures with an extremely low coordination number of four. Most other cubic and hexagonal solids have a nearest neighbor coordination of twelve. This low coordination is the result of the directional H-bonds in the tetrahe-

dral coordination. If, on the other hand, we have more isotropic interactions the system should approach a normal condensed system with much higher coordination. This is seen in the structure of both high-density amorphous ice (HDA) and crystalline high-pressure ices where the tetrahedral next-nearest distance of 4.5 Å collapses inward to shorter distances; indeed, the similarity between the pair-correlation functions of HDA and liquid water was noted already by Narten and coworkers [172]. This leads to higher coordination at longer distances than in the tetrahedral structure and thereby also to higher density. We envisage that the HDL structure is similar to the high-pressure ices in terms of the second shell that moves inwards from the tetrahedral distances as discussed above, which is also consistent with the 3.6 Å second-shell position predicted by the linear relationship in XAS/XRS between main- to post-edge ratio in fig. 11a.

The high-pressure ices still have a mostly four-coordinated structure in terms of nearest neighbor distances which, with the inward collapse of the second shell, leads to densities well above liquid water. What makes HDL have a density significantly lower than for the high-pressure ices is that the first shell is distorted in order to allow thermal excitation of librational modes. We here propose that these distortions are not symmetrical but instead asymmetrical in order to minimize loss of enthalpy leading to a doubly H-bonded local structure in alignment with recently published *ab initio* studies [95, 173]. It turns out that the H-bond energy is maximized when there is an equal number of donor and acceptor bonds and a particularly favorable situation in terms of energy per H-bond is when each molecule forms only one bond of each kind [174]. This would lead to a stabilization of doubly H-bonded structures which interact with the surrounding through more isotropic forces and gain entropy since the librational modes would become thermally accessible.

Such a picture is supported based on thermodynamic grounds where it has been argued that over a large range of the liquid-vapor coexistence line the averaged water interaction potential should resemble that of liquid Argon, *i.e.* H-bonding is not dominating resulting in mostly a doubly H-bonded structure [175]. Furthermore, a model from 1973 suggests, also based on thermodynamic arguments, that the H-bonding structure upon melting of ice should mostly correspond to breaking of H-bonds between rings in the tetrahedral ice structure while keeping the internal ring structure intact [176]. This would also lead to a local doubly H-bonded picture.

We can test the hypothesis regarding the distortions in the first shell by analyzing the O-O correlation in a separation between HDL- and LDL-like local structures in the liquid. In fig. 32 we show O-O PCF:s from simulated TIP4P/2005 water where the PCFs are constructed based on the LSI index of water molecules in the real structure using different cut-offs; the PCFs are constructed between like species with the cross-correlation shown separately.

With the high cut-off above $I = 0.05\,\text{Å}^2$ (fig. 32, top) we focus on subspecies in the simulation with a very tetrahedral local, LDL-like, environment which is evident from the very structured PCF of the component above the cut-off. The species with I-values below cut-off exhibit a much less structured PCF with a filling in of intensity between the first and second shell. Going to the lower cut-off (fig. 32, middle) we select the other extreme below this cut-off, *i.e.* molecules with a more HDL-like disordered environment. We make two important observations; 1) the filling out of the region between the first and second shell becomes strongly enhanced and 2) the height of the first peak of the species below cut-off goes down compared to fig. 32 (top), which means that the enhanced intensity between the first and second shells is due to molecules in both the first and second shell moving into this region for these species.

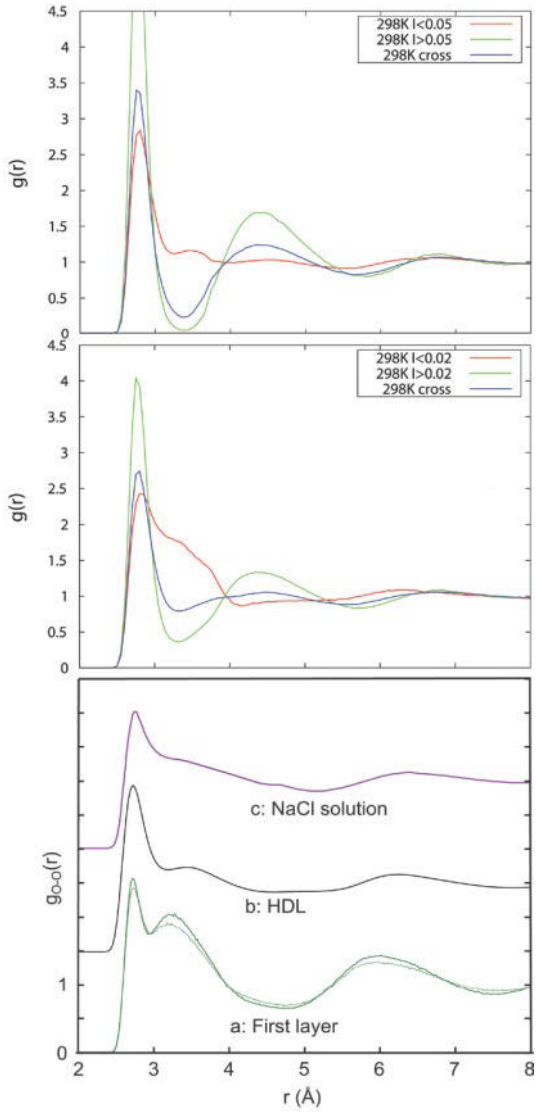

Fig. 32. – Pair-correlation functions of TIP4P/2005 water at 298 K separated into PCFs between molecules with LSI value above and below a threshold and their cross-correlation. The threshold is set to $0.05\,\text{Å}^2$ (top) and $0.02\,\text{Å}^2$ (middle) showing extremes of LDL-like and HDL-like components, respectively, in the simulation. Bottom: Comparison of PCF for simulated first-layer water on a BaF_2 substrate [20] with experimentally derived PCF for HDL water [14] and O-O PCF of water in NaCl solution [177].

It is interesting to compare to the PCF of HDL (fig. 32 bottom, b) which has been derived from neutron diffraction data taken at different pressures and temperatures [14] and to the O-O PCF of water in salt solution (fig. 32 bottom, c) [177]. Both show a significant filling in of the region between the first and second shell and also a reduced height of the first O-O correlation similar to the low-LSI component in the top two panels

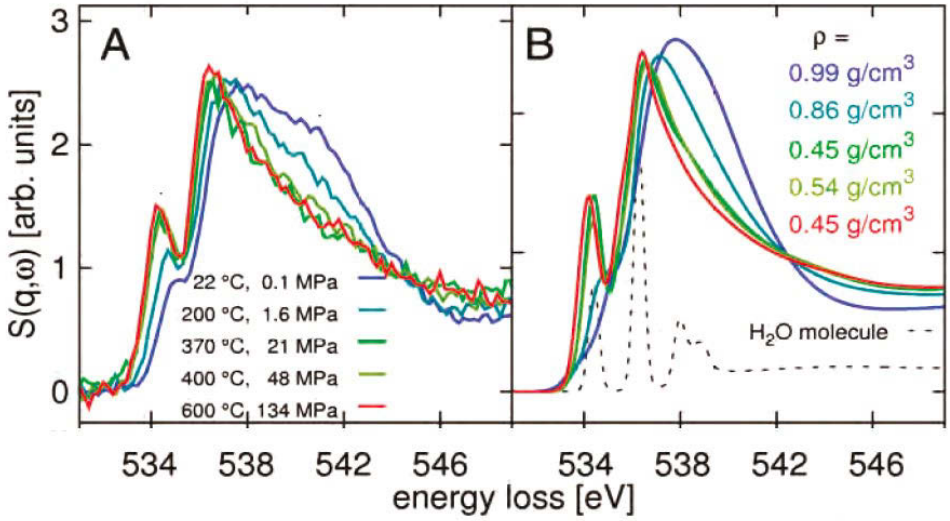

Fig. 33. – (a) O K-edge XRS spectra of water at different pressures and temperatures along the liquid-gas coexistence curve and at ambient conditions. (b) Calculated spectra for similar temperatures and densities as the experimental spectra and for the water monomer. Reproduced from ref. [178].

of fig. 32. We also note the close similarity to the PCF of the first layer of simulated water on $BaF_2(111)$ (fig. 32 bottom, a) [20] which also experimentally has been characterized as HDL-like based on the near-absence of post-edge in XAS spectra at ambient and even down to deeply supercooled conditions. An important observation is thus that the filling out of the region between the first and second shells has contributions both from the first and second neighbors, which is fully consistent with a picture of closer packing in the HDL-like component where a symmetric donor-acceptor H-bond situation is maintained while the other two molecules from a tetrahedral local structure move out to accommodate the approach of molecules from the second shell.

It is interesting to look at experiments on water when the conditions are well above the transition region between anomalous and normal liquid behavior, as shown in fig. 2. At high temperatures we would expect that the local water structure becomes pure HDL. Let us in this context return to the XAS/XRS of water as discussed in sect. **2**. Figure 33a shows XRS spectra for hot water at temperatures above the boiling point following the liquid-gas coexistence curve in comparison with the spectrum at ambient conditions [178]. If we look at the spectrum at 473 K (200 °C in the figure) and a density of 0.86 g/cm^3 we note that the post-edge feature is gone while the pre-edge peak intensity is increased and the peak shifted to lower energy. This follows nicely the trend in fig. 7a but here going to much higher temperatures. The disappearance of the post-edge indicates that the tetrahedral patches have been lost completely giving the appearance of a normal liquid. Figure 33b shows spectrum calculations [178] using the transition potential approximation [87] that has been shown to give excellent agreement with both gas phase water and hexagonal ice. The structures were generated based on *ab initio* MD simulations with a traditional functional without van der Waals interactions [178]. The

computed spectrum at $0.86\,\mathrm{g/cm^3}$ shows the lack of post-edge structures and except for slightly too low pre-edge intensity gives a reasonable agreement with the experimental spectrum. Analysis of the structures in the simulation showed predominantly molecules with two H-bonds. This is thus a spectrum of a local HDL class of structure showing strong pre- and main-edge and lack of a clear, distinct post-edge. That there is a sloping intensity in the post-edge region reflects that there are still H-bonds in the local structure but not leading to the well-defined peak seen for tetrahedral structures.

As the temperature is raised further, the spectra in fig. 33a approach more and more the gas phase spectrum with shift to lower energy for both the pre- and main-edges coupled with increased intensity. In particular the main-edge becomes nearly as sharp as in the gas phase and the sloping background in the post-edge region becomes much less. The spectrum calculations of the structures from the MD simulations give the right trend with a lack of post-edge and analysis of the local structures shows a significant reduction in H-bonding. Here the HDL structure becomes so highly thermally excited that even the doubly H-bonded structure gets lost. There are highly excited librational vibrational modes where the molecules are mostly free to rotate in a non-H-bonded environment.

One thing that is interesting to note is that the spectrum computed from the structures of the MD simulations at ambient conditions is far from the experimental spectrum. There is a lack of pre-edge intensity and the main- and post-edges have merged into a broad structure at 538 eV. This was also observed using the transition potential approximation to compute spectra of structures from SPC/E water at ambient conditions [3]. The computed spectra are in good agreement with experiment when water is in the range of normal liquid conditions but not in the anomalous transition region. This indicates that indeed many MD simulations, using either classical force-fields or *ab initio* with traditional functionals, give a structure more like an average between HDL- and LDL-like for water in the regime of the temperature-pressure phase diagram where properties become anomalous in accordance with the discussion of isothermal compressibility, computed XAS and SAXS in sects. **3** and **4**.

9. – Concluding remarks

We have in this chapter presented a picture of water that unifies many ideas discussed in the supercooled regime with recent results obtained from various X-ray spectroscopic and scattering experiments and molecular dynamics simulations at ambient conditions. Here we summarize our findings in a simple picture related to the cartoon shown in fig. 3. At temperatures close to the boiling point, water behaves as a simple liquid where most interactions are isotropic and dominated by van der Waals interactions. This is a local structure where most molecules are in strongly disordered environments with no well-defined separation between the 1st and 2nd shell. This type of non-directional bonding gives high flexibility for various vibrational motions and thereby high entropy.

As the liquid cools down the water molecules start to stick to each other through directional H-bonds. This will appear in two classes of configurations, tetrahedral and asymmetric, with fluctuations between them on some short time-scale. When participating in a fluctuation into a tetrahedral structure each molecule is involved in four strong hydrogen bonds which minimizes the enthalpy, *i.e.* a locally favored structure [179, 180]. Since cooperativity effects make the bonds stronger if water is bonded to other waters that are also in a tetrahedral structure, a fluctuation into a tetrahedral structure expands into a small local region. Since the molecules are directionally bonded with four bonds

the librational motion becomes restricted and thereby contributes only weakly to the entropy.

The other class of structures that is formed we can call asymmetric local coordination with fewer, but paired, donor-acceptor H-bonds. Here the energy per H-bond is higher than in the tetrahedral structures but since there are fewer directional H-bonds there is less enthalpic stabilization. With less directional H-bonds there is more flexibility for librational and translational motions and thereby a higher entropy. The OH groups that are involved in either a strong or weak H-bond can switch on a very fast time scale. In this structure isotropic molecular van der Waals interactions are important causing interstitial molecules to come in from a collapsed 2nd shell and also distortions around the 1st shell. Since there are more water molecules in the first coordination shell (defined out to 3.5 Å rather than to the minimum in $r^2 g_{\mathrm{OO}}(r)$ at 3.30 Å) than in the tetrahedral structures we call these high-density liquid (HDL) structures. Another way of viewing such species is that we start not with hexagonal ice but with high-density amorphous (HDA) or very high-density amorphous (VHDA) ices where we have a large collapse of the second shell. In these ices we also have a local tetrahedral bonding but with other angles towards the second shell (often called interstitials). With increasing temperature, we induce asymmetric distortions around these tetrahedrally bonded molecules in the first shell while keeping the interstitials.

There are fluctuations between the tetrahedral structures and asymmetric or high-density structures. As we cool the liquid down the molecules in the asymmetric structures fluctuate more and more frequently into tetrahedral structures which grow in size since the balance between enthalpy and entropy in the free energy shifts more and more to favor enthalpy with decreasing temperature. The timescale in the fluctuations between these two classes should furthermore slow down. There is also a continuous change in the asymmetric/high density with temperature. The switching time of OH-groups between strong and weak/broken H-bonding is expected to slow down and thereby also the amplitude in the motion with decreasing temperature. We will be approaching more and more a local arrangement with four strong H-bonds. However, not as in hexagonal ice, but more towards high-density ices with still many interstitials. That the density decreases below 4 °C is simply due to that we are at the same time converting many molecules into tetrahedral, LDL-like, structures more similar to hexagonal ice but disordered towards low-density amorphous ice with the second shell at the tetrahedral angle causing an open network with low density. In this picture we have to consider both these two classes of fluctuations (between tetrahedral and asymmetric and within asymmetric) separately but most likely there should also be some coupling.

All of the experimental information presented here is consistent with the above hypothesis but we need to complement these with results from simulations. We have shown that the local structure index (LSI) [116,117] distribution based on the inherent structure in simulations with the TIP4P/2005 model is strictly bimodal in the distribution between HDL- and LDL-like local structures [24] and the ratio between the two adheres closely to estimates from XAS [18] and XES [15,23]. In addition, the changes with temperature of the distribution in the inherent structure mimic closely what is observed in XAS, XES as well as in OH stretch vibrational Raman spectroscopy of liquid water where in all cases the features corresponding to tetrahedral, LDL-like structures are seen to vary in intensity with temperature, but stay at fixed position. The features due to the HDL-like structure, on the other hand, are seen to shift in position with temperature in addition to the variation in intensity due to conversion between LDL- and HDL-like species. This holds true also for SPC/E water [118,119] and we speculate that this should be a gen-

eral property of the inherent structure of force-fields and *ab initio* techniques that give a reasonable representation of water. However, when the simulations are run at finite temperature the bimodality is largely washed out, except in the deeply supercooled region where there are reports of fluctuations between HDL and LDL liquid [36, 114]. On the other hand, in the important ambient regime, where most processes relevant to life, chemistry and geochemistry occur, the bimodality observed experimentally is not reproduced by simulations. It seems that the underlying potential energy surface on which the simulations move is not sufficiently corrugated and more of an average structure is obtained.

We have in the present chapter discussed effects that are necessary to include in a simulation that realistically mimics real water in terms of structure and fluctuations and deduced lower bounds on simulation size based on experimental observations. These include the important electronic structure cooperativity effects which lead to a strengthening of H-bonds if they form part of a chain or network with balanced contributions from donors and acceptors, *i.e.* for each molecule an equal number of acceptors and donors; this will enhance the growth of tetrahedral regions as evidenced by DFT simulations that neglect dispersion or van der Waals effects giving a very LDL-like liquid [19]. Note here that, although polarizable force-fields introduce more flexibility and can give improvements, the charge redistributions in a molecule upon H-bond formation go against expectation from electrostatics; the accepting lone-pair polarizes away from the donating proton in order to minimize Pauli repulsion which allows a closer approach and enhanced electrostatic interaction [129]. Introducing the more isotropic van der Waals interaction through non-local correlation functionals in DFT simulations balances the directional H-bonding and leads to a softer structure and even to a collapse into strongly HDL-like structure [19, 132] demonstrating that the HDL-like minimum has been too strongly enhanced. However, there are two additional effects to consider where one is the common protocol to run simulations in the NVT ensemble assuming the experimental density together with the size of the simulation box; assuming the HDL type structures dominate at ambient conditions the density is mainly determined by this component and fluctuations into larger LDL-like environments will be prevented by the effective pressure from the simulation box. For a large enough box this pressure penalty can be small, but the experimental observation of shell-structure out to $\sim 14\,\text{Å}$ from X-ray diffraction [157] in accordance with estimates from SAXS [15] would imply that significantly larger simulation boxes than commonly used in *ab initio* MD simulations should be used and preferably in the NpT ensemble to allow the entire box to convert; note that at ambient conditions a simulation box of 64 molecules corresponds to a box side of 12.44 Å. The other effect to include is the effects of the quantum nature of hydrogen which manifests as significant differences in macroscopic properties of H_2O and D_2O water. In terms of HDL and LDL quantum effects strengthen strong and weaken weak H-bonds [133] which can be expected to enhance the asymmetry between H-bonded and non–H-bonded OH in the HDL species. Including quantum effects furthermore discriminates between HDL and LDL in the free energy contributions since for tetrahedrally H-bonded LDL species the classically allowed thermal excitation of librational modes becomes prohibited due to the too large quantum level-spacing. All of these effects must be simultaneously accounted for and included at a sufficiently high level to definitely determine in simulations the delicate balance between structural components in real liquid water. This is a challenge, but understanding water is a major scientific goal.

* * *

We acknowledge Basic Energy Sciences (BES) through the Stanford Synchrotron Radiation Lightsource (SSRL), and the Swedish Research Council for financial support. The results discussed in the present chapter have naturally been obtained in collaboration with a large number of extraordinary scientists who have worked very dedicatedly on these, many times very difficult, problems. All have been essential to this effort but C. Benmore, U. Bergmann, M. Cavalleri, C. Chen, Y. Harada, C. Huang, N. Huang, M. Leetmaa, M.P. Ljungberg, T. McQueen, S. Myneni, A. Møgelhøj, D. Nordlund, L. Å. Näslund, M. Odelius, H. Ogasawara, J. Sellberg, L. B. Skinner, O. Takahashi, T. Tokushima, I. Waluyo, Ph. Wernet and K. T. Wikfeldt deserve special credit.

REFERENCES

[1] Chaplin M. F., *Water Structure and Behavior* `http://www.lsbu.ac.uk/water/index.html`.
[2] Ball P., *Chem. Rev.*, **108** (2008) 74.
[3] Nilsson A., Nordlund D., Waluyo I., Huang N., Ogasawara H., Kaya S., Bergmann U., Näslund L.-Å., Öström H., Wernet P., Andersson K. J., Schiros T. and Pettersson L. G. M., *J. Electron. Spectrosc. Relat. Phenom.*, **177** (2010) 99.
[4] Debenedetti P. G., *J. Phys.: Condens. Matter*, **15** (2003) R1669.
[5] Landau L. D. and Lifshitz E. M., *Statistical Physics*, Part 1 (Butterworth-Heinemann, Oxford) 1980.
[6] Kumar P., Han S. and Stanley H. E., *J. Phys.: Condens. Matter*, **21** (2009) 504108.
[7] Speedy R. J. and Angell C. A., *J. Chem. Phys.*, **65** (1976) 851.
[8] Kanno H. and Angell C. A., *J. Chem. Phys.*, **70** (1979) 4008.
[9] Hare D. E. and Sorensen C. M., *J. Chem. Phys.*, **84** (1986) 5085.
[10] Zheleznyi B. V., *Russ. J. Phys. Chem.*, **43** (1969) 1311.
[11] Wikfeldt K. T., Huang C., Nilsson A. and Pettersson L. G. M., *J. Chem. Phys.*, **134** (2011) 214506.
[12] Mallamace F., Broccio M., Corsaro C., Faraone A., Majolino D., Venuti V., Liu L., Mou C. and Chen S., *Proc. Natl. Acad. Sci. U.S.A.*, **104** (2007) 424.
[13] Mallamace F., Corsaro C. and Stanley H. E., *Sci. Rep.*, **2** (2012) 993.
[14] Soper A. K. and Ricci M. A., *Phys. Rev. Lett.*, **84** (2000) 2881.
[15] Huang C., Wikfeldt K. T., Tokushima T., Nordlund D., Harada Y., Bergmann U., Niebuhr M., Weiss T. M., Horikawa Y., Leetmaa M., Ljungberg M. P., Takahashi O., Lenz A., Ojamäe L., Lyubartsev A. P., Shin S., Pettersson L. G. M. and Nilsson A., *Proc. Natl. Acad. Sci. U.S.A.*, **106** (2009) 15214.
[16] Nilsson A., Huang C. and Pettersson L. G. M., *J. Mol. Liq.*, **176** (2012) 2.
[17] Nilsson A. and Pettersson L. G. M., *Chem. Phys.*, **389** (2011) 1.
[18] Wernet P., Nordlund D., Bergmann U., Cavalleri M., Odelius M., Ogasawara H., Näslund L. Å., Hirsch T. K., Ojamäe L., Glatzel P., Pettersson L. G. M. and Nilsson A., *Science*, **304** (2004) 995.
[19] Møgelhøj A., Kelkkanen A., Wikfeldt K. T., Schiøtz J., Mortensen J. J., Pettersson L. G. M., Lundqvist B. I., Jacobsen K. W., Nilsson A. and Nørskov J. K., *J. Phys. Chem. B*, **115** (2011) 14149.
[20] Kaya S., Yamamoto S. D. S., Newberg J. T., Bluhm H., Ogasawara H., Kendelewicz T., Brown G. E., Pettersson L. G. M. and Nilsson A., *Sci. Rep.*, **3** (2012) 1074.
[21] Huang C., Weiss T. M., Nordlund D., Wikfeldt K. T., Pettersson L. G. M. and Nilsson A., *J. Chem. Phys.*, **133** (2010) 134504.
[22] Huang C., Wikfeldt K. T., Nordlund D., Bergmann U., McQueen T., Sellberg J., Pettersson L. G. M. and Nilsson A., *Phys. Chem. Chem. Phys.*, **13** (2011) 19997.

[23] Tokushima T., Harada Y., Takahashi O., Senba Y., Ohashi H., Pettersson L. G. M., Nilsson A. and Shin S., *Chem. Phys. Lett.*, **460** (2008) 387.
[24] Wikfeldt K. T., Nilsson A. and Pettersson L. G. M., *Phys. Chem. Chem. Phys.*, **13** (2011) 19918.
[25] Overduin S. D. and Patey G. N., *J. Phys. Chem. B*, **116** (2012) 12014.
[26] Taschin A., Bartolini P., Eramo R., Righini R. and Torre R., *Nat. Commun.*, **4** (2013) 2401.
[27] Mallamace F., Corsaro C. and Stanley H. E., *Proc. Natl. Acad. Sci. U.S.A.*, **110** (2013) 4899.
[28] Clark G. N. I., Cappa C. D., Smith J. D., Saykally R. J. and Head-Gordon T., *Mol. Phys.*, **108** (2010) 1415.
[29] Clark G. N. I., Hura G., Teixeira J., Soper A. K. and Head-Gordon T., *Proc. Natl. Acad. Sci. U.S.A.*, **107** (2010) 14003.
[30] Poole P. H., Sciortino F., Essmann U. and Stanley H. E., *Nature*, **360** (1992) 324.
[31] Mishima O. and Stanley H. E., *Nature*, **396** (1998) 329.
[32] Mishima O., *J. Chem. Phys.*, **133** (2010) 144503.
[33] Mishima O. and Stanley H. E., *Nature*, **392** (1998) 164.
[34] Limmer D. T. and Chandler D., *J. Chem. Phys.*, **135** (2011) 134503.
[35] Moore E. B. and Molinero V., *Nature*, **479** (2011) 506.
[36] Kesselring T. A., Franzese G., Buldyrev S. V., Herrmann H. J. and Stanley H. E., *Sci. Rep.*, **2** (2012) 474.
[37] Liu Y., Palmer J. C., Panagiotopoulos A. Z. and Debenedetti P. G., *J. Chem. Phys.*, **137** (2012) 214505.
[38] Poole P. H., Becker S. R., Sciortino F. and Starr F. W., *J. Phys. Chem. B*, **115** (2011) 14176.
[39] Sciortino F., Saika-Voivod I. and Poole P. H., *Phys. Chem. Chem. Phys.*, **13** (2011) 19759.
[40] Myneni S., Luo Y., Näslund L.-Å., Cavalleri M., Ojamäe L., Ogasawara H., Pelmenschikov A., Wernet P., Väterlein P., Heske C., Hussain Z., Pettersson L. G. M. and Nilsson A., *J. Phys.: Condens. Matter*, **14** (2002) L213.
[41] Bergmann U., Wernet P., Glatzel P., Cavalleri M., Pettersson L. G. M., Nilsson A. and Cramer S. P., *Phys. Rev. B*, **66** (2002) 092107.
[42] Fuchs O., Zharnikov M., Weinhardt L., Blum M., Weigand M., Zubavichus Y., Bär M., Maier F., Denlinger J. D., Heske C., Grunze M. and Umbach E., *Phys. Rev. Lett.*, **100** (2008) 027801.
[43] Guo J. H., Luo Y., Augustsson A., Rubensson J. E., Såthe C., Ågren H., Siegbahn H. and Nordgren J., *Phys. Rev. Lett.*, **89** (2002) 137402.
[44] Nilsson A., Tokushima T., Horikawa Y., Harada Y., Ljungberg M. P., Shin S. and Pettersson L. G. M., *J. Electron. Spectrosc. Relat. Phenom.*, **188** (2013) 84.
[45] Gilberg E., Hanus M. J. and Foltz B., *J. Chem. Phys.*, **76** (1982) 5093.
[46] Weinhardt L., Benkert A., Meyer F., Blum M., Wilks R. G., Yang W., Bär M., Reinert F. and Heske C., *J. Chem. Phys.*, **136** (2012) 144311.
[47] Lange K. M., Könecke R., Ghadimi S., Golnak R., Soldatov M. A., Hodeck K. F., Soldatov A. and Aziz E. F., *Chem. Phys.*, **377** (2010) 1.
[48] Nordlund D., Odelius M., Bluhm H., Ogasawara H., Pettersson L. G. M. and Nilsson A., *Chem. Phys. Lett.*, **460** (2008) 86.
[49] Winter B., Weber R., Widdra W., Dittmar M., Faubel M. and Hertel I. V., *J. Phys. Chem. A*, **108** (2004) 2625.
[50] Winter B. and Faubel M., *Chem. Rev.*, **106** (2006) 1176.
[51] Neeb M., Rubensson J. E., Biermann M. and Eberhardt W., *J. Electron. Spectrosc. Relat. Phenom.*, **67** (1994) 261.
[52] Nibbering E. T. J. and Elsaesser T., *Chem. Rev.*, **104** (2004) 1887.
[53] Ljungberg M. P., Pettersson L. G. M. and Nilsson A., *J. Chem. Phys.*, **134** (2011) 044513.

[54] Odelius M., Ogasawara H., Nordlund D., Fuchs O., Weinhardt L., Maier F., Umbach E., Heske C., Zubavichus Y., Grunze M., Denlinger J. D., Pettersson L. G. M. and Nilsson A., *Phys. Rev. Lett.*, **94** (2005) 227401.
[55] Nordlund D., Ogasawara H., Andersson K. J., Tatarkhanov M., Salmerón M., Pettersson L. G. M. and Nilsson A., *Phys. Rev. B*, **80** (2009) 233404.
[56] Iannuzzi M., *J. Chem. Phys.*, **128** (2008) 204506.
[57] Odelius M., Cavalleri M., Nilsson A. and Pettersson L. G. M., *Phys. Rev. B*, **73** (2006) 024205.
[58] Prendergast D. and Galli G., *Phys. Rev. Lett.*, **96** (2006) 215502.
[59] Smith J. D., Cappa C. D., Wilson K. R., Messer B. M., Cohen R. C. and Saykally R. J., *Science*, **306** (2004) 851.
[60] Liang L., Rulis P., Ouyang L. Z. and Ching W. Y., *Phys. Rev. B*, **83** (2011) 024201.
[61] Wikfeldt K. T., Leetmaa M., Ljungberg M. P., Nilsson A. and Pettersson L. G. M., *J. Phys. Chem. B*, **113** (2009) 6246.
[62] Leetmaa M., Wikfeldt K. T., Ljungberg M. P., Odelius M., Swenson J., Nilsson A. and Pettersson L. G. M., *J. Chem. Phys.*, **129** (2008) 084502.
[63] Bellissent-Funel M. C., *Europhys. Lett.*, **42** (1998) 161.
[64] Nordlund D., Ogasawara H., Bluhm H., Takahashi O., Odelius M., Nagasono M., Pettersson L. G. M. and Nilsson A., *Phys. Rev. Lett.*, **99** (2007) 217406.
[65] Pylkkänen T., Sakko A., Hakala M., Hämäläinen K., Monaco G. and Huotari S., *J. Phys. Chem. B*, **115** (2011) 14544.
[66] Waluyo I., Huang C., Nordlund D., Bergmann U., Weiss T. M., Pettersson L. G. M. and Nilsson A., *J. Chem. Phys.*, **134** (2011) 064513.
[67] Corradini D., Rovere M. and Gallo P., *J. Chem. Phys.*, **132** (2010) 134508.
[68] Corradini D., Rovere M. and Gallo P., *J. Phys. Chem. B*, **115** (2011) 1461.
[69] Geissler P. L., *J. Am. Chem. Soc.*, **127** (2005) 14930.
[70] Smith J. D., Cappa C. D., Wilson K. R., Cohen R. C., Geissler P. L. and Saykally R. J., *Proc. Natl. Acad. Sci. U.S.A.*, **102** (2005) 14171.
[71] Sun Q., *Vib. Spectrosc.*, **62** (2012) 110.
[72] Sun Q., *Chem. Phys. Lett.*, **568-569** (2013) 90.
[73] Walrafen G. E., *J. Chem. Phys.*, **120** (2004) 4868.
[74] Walrafen G. E., *J. Chem. Phys.*, **121** (2004) 2729.
[75] Walrafen G. E., Fisher M. R., Hokmabadi M. S. and Yang W.-H., *J. Chem. Phys.*, **85** (1986) 6970.
[76] Walrafen G. E., Hokmabadi M. S. and Yang W.-H., *J. Chem. Phys.*, **85** (1986) 6964.
[77] Walrafen G. E. and Pugh E., *J. Solut. Chem.*, **33** (2004) 81.
[78] Bakker H. J. and Skinner J. L., *Chem. Rev.*, **110** (2010) 1498.
[79] Liu J., Andino R. S., Miller C. M., Chen X., Wilkins D. M., Ceriotti M. and Manolopoulos D. E., *J. Phys. Chem. C*, **117** (2013) 2944.
[80] Nagata Y., Pool R. E., Backus E. H. G. and Bonn M., *Phys. Rev. Lett.*, **109** (2012) 226101.
[81] Harada Y., Tokushima T., Horikawa Y., Takahashi O., Niwa H., Kobayashi M., Oshima M., Senba Y., Ohashi H., Wikfeldt K. T., Nilsson A., Pettersson L. G. M. and Shin S., *Phys. Rev. Lett.*, **111** (2013) 193001.
[82] Ogasawara H., Brena B., Nordlund D., Nyberg M., Pelmenschikov A., Pettersson L. G. M. and Nilsson A., *Phys. Rev. Lett.*, **89** (2002) 276102.
[83] Haq S., Clay C., Darling G. R., Zimnitas G. and Hodgson A., *Phys. Rev. B*, **73** (2006) 115414.
[84] Andersson K., Nikitin A., Pettersson L. G. M., Nilsson A. and Ogasawara H., *Phys. Rev. Lett.*, **93** (2004) 196101.
[85] Nordlund D., Ogasawara H., Wernet P., Nyberg M., Odelius M., Pettersson L. G. M. and Nilsson A., *Chem. Phys. Lett.*, **395** (2004) 161.
[86] Mitsui T., Rose M. K., Fomin E., Ogletree D. F. and Salmerón M., *Science*, **297** (2002) 1850.

[87] Leetmaa M., Ljungberg M. P., Lyubartsev A. P., Nilsson A. and Pettersson L. G. M., *J. Electron. Spectrosc. Relat. Phenom.*, **177** (2010) 135.
[88] Cavalleri M., Ogasawara H., Pettersson L. G. M. and Nilsson A., *Chem. Phys. Lett.*, **364** (2002) 363.
[89] Nyberg M., Hasselström J., Karis O., Wassdahl N., Weinelt M., Nilsson A., Pettersson L. G. M., *J. Chem. Phys.*, **112** (2000) 5420.
[90] Nyberg M., Odelius M., Pettersson L. G. M. and Nilsson A., *J. Chem. Phys.*, **119** (2003) 12577.
[91] Hasselström J., Karis O., Nyberg M., Pettersson L. G. M., Weinelt M., Wassdahl N. and Nilsson A., *J. Phys. Chem. B*, **104** (2000) 11480.
[92] Pettersson L. G. M., Nilsson A., Myneni S., Luo Y., Nyberg M., Cavalleri M., Ojamäe L., Näslund L. Å., Ogasawara H., Odelius M. and Pelmenschikov A., *J. Synchr. Radiat.*, **8** (2001) 136.
[93] Schiros T., Ogasawara H., Takahashi O., Öström H., Andersson K., Pettersson L. G. M., Nilsson A., Haq S. and Hodgson A., *Chem. Phys. Lett.*, **429** (2006) 415.
[94] Schiros T., Näslund L.-Å., Andersson K., Gyllenpalm J., Karlberg G. S., Odelius M., Ogasawara H., Pettersson L. G. M. and Nilsson A., *J. Phys. Chem. C*, **111** (2007) 15003.
[95] Kühne T. D. and Khaliullin R. Z., *Nat. Commun.*, **4** (2013) 1450.
[96] Pylkkänen T., Giordano V. M., Chervin J.-C., Sakko A., Hakala M., Soininen J. A., Hämäläinen K., Monaco G. and Huotari S., *J. Phys. Chem. B*, **114** (2010) 3804.
[97] Stöhr J., Sette F. and Johnson A. L., *Phys. Rev. Lett.*, **53** (1984) 1684.
[98] Cavalleri M., Näslund L.-Å., Edwards D. C., Wernet P., Ogasawara H., Myneni S., Ojamäe L., Odelius M., Nilsson A. and Pettersson L. G. M., *J. Chem. Phys.*, **124** (2006) 194508.
[99] Minceva-Sukarova B., Sherman W. F. and Wilkinson G. R., *J. Phys. C: Solid State Phys.*, **17** (1984) 5833.
[100] Anderson P. W., *Phys. Rev.*, **124** (1961) 41.
[101] Newns D. M., *Phys. Rev.*, **178** (1969) 1123.
[102] Chen W., Wu X. and Car R., *Phys. Rev. Lett.*, **105** (2010) 017802.
[103] Kong L., Wu X. and Car R., *Phys. Rev. B*, **86** (2012) 134203.
[104] Hetényi B., De Angelis F., Giannozzi P. and Car R., *J. Chem. Phys.*, **120** (2004) 8632.
[105] Zubavichus Y., Yang Y., Zharnikov M., Fuchs O., Schmidt T., Heske C., Umbach E., Tzvetkov G., Netzer F. P. and Grunze M., *Chem. Phys. Chem.*, **5** (2004) 509.
[106] Cavalleri M., Odelius M., Nordlund D., Nilsson A. and Pettersson L. G. M., *Phys. Chem. Chem. Phys.*, **7** (2005) 2854.
[107] Triguero L., Pettersson L. G. M. and Ågren H., *Phys. Rev. B*, **58** (1998) 8097.
[108] Thürmer S., Ončák M., Ottosson N., Seidel R., Hergenhahn U., Bradforth S. E., Slavíček P. and B. Winter, *Nat. Chem.*, **5** (2013) 590.
[109] Pettersson L. G. M., *Nat. Chem.*, **5** (2013) 553.
[110] Vinson J., Kas J. J., Rehr J. J., Vila F. D. and Shirley E. L., *Phys. Rev. B*, **85** (2012) 045101.
[111] Ekström U., Norman P., Carravetta V. and Ågren H., *Phys. Rev. Lett.*, **97** (2006) 143001.
[112] Fransson T., Coriani S., Christiansen O. and Norman P., *J. Chem. Phys.*, **138** (2013) 124311.
[113] Stokely K., Mazza M. G., Stanley H. E. and Franzese G., *Proc. Natl. Acad. Sci. U.S.A.*, **107** (2010) 1301.
[114] Cuthbertson M. J. and Poole P. H., *Phys. Rev. Lett.*, **106** (2011) 115706.
[115] Kesselring T. A., Franzese G., Buldyrev S. V., Herrmann H. J. and Stanley H. E., *Sci. Rep.*, **2** (2012) 474.
[116] Shiratani E.and Sasai M., *J. Chem. Phys.*, **108** (1998) 3264.
[117] Shiratani E. and Sasai M., *J. Chem. Phys.*, **104** (1996) 7671.

[118] Accordino S. R., Rodriguez Friz J. A., Sciortino F. and Appignanesi G. A., *Eur. Phys. J. E*, **34** (2011) 48.
[119] Appignanesi G. A., Rodriguez Friz J. A. and Sciortino F., *Eur. Phys. J. E*, **29** (2009) 305.
[120] Debenedetti P. G. and Stillinger F. H., *Nature*, **410** (2001) 259.
[121] Abascal J. L. F. and Vega C., *J. Chem. Phys.*, **123** (2005) 234505.
[122] Tokushima T., Harada Y., Horikawa Y., Takahashi O., Senba Y., Ohashi H., Pettersson L. G. M., Nilsson A. and Shin S., *J. Electron. Spectrosc. Relat. Phenom.*, **177** (2010) 192.
[123] Xu L., Kumar P., Buldyrev S. V., Chen S.-H., Poole P. H., Sciortino F. and Stanley H. E., *Proc. Natl. Acad. Sci. U.S.A.*, **102** (2005) 16558.
[124] Simeoni G. G., Bryk T., Gorelli F. A., Krisch M., Ruocco G., Santoro M. and Scopigno T., *Nat. Phys.*, **6** (2010) 503.
[125] Abascal J. L. F. and Vega C., *J. Chem. Phys.*, **133** (2010) 234502.
[126] Xu L., Mallamace F., Yan Z., Starr F. W., Buldyrev S. V. and Stanley H. E., *Nat. Phys.*, **5** (2009) 565.
[127] Huang C., Wikfeldt K. T., Tokushima T., Nordlund D., Harada Y., Bergmann U., Niebuhr M., Weiss T. M., Horikawa Y., Leetmaa M., Ljungberg M. P., Takahashi O., Lenz A., Ojamäe L., Lyubartsev A., Shin S., Pettersson L. G. M. and Nilsson A., *Proc. Natl. Acad. Sci. U.S.A.*, **107** (2010) E45.
[128] Ojamäe L. and Hermansson K., *J. Phys. Chem.*, **98** (1994) 4271.
[129] Nilsson A., Ogasawara H., Cavalleri M., Nordlund D., Nyberg M., Wernet P. and Pettersson L. G. M., *J. Chem. Phys.*, **122** (2005) 154505.
[130] Yoo S., Zeng X. and Xantheas S. S., *J. Chem. Phys.*, **130** (2009) 221102.
[131] Yoo S. and Xantheas S. S., *J. Chem. Phys.*, **134** (2011) 121105.
[132] Wang J., Román-Pérez G., Soler J. M., Artacho E. and Fernández-Serra M.-V., *J. Chem. Phys.*, **134** (2011) 024516.
[133] Li X.-Z., Walker B. and Michaelides A., *Proc. Natl. Acad. Sci. U.S.A.*, **108** (2011) 6369.
[134] Angell C. A., Sichina W. J. and Oguni M., *J. Phys. Chem.*, **86** (1982) 998.
[135] Conde O., Teixeira J. and Papon P., *J. Chem. Phys.*, **76** (1982) 3747.
[136] Pi H. L., Aragones J. L., Vega C., Noya E. G., Abascal J. L. F., Gonzalez M. A. and McBride C., *Mol. Phys.*, **107** (2009) 365.
[137] Saul A. and Wagner W., *J. Phys. Chem. Ref. Data*, **18** (1989) 1537.
[138] English N. J. and Tse J. S., *Phys. Rev. Lett.*, **106** (2011) 037801.
[139] Brovchenko I., Geiger A. and Oleinikova A., *J. Chem. Phys.*, **123** (2005) 044515.
[140] Kumar P., Wikfeldt K. T., Schlesinger D., Pettersson L. G. M. and Stanley H. E., *Sci. Rep.*, **3** (2013) 1980.
[141] Geiger A. and Stanley H. E., *Phys. Rev. Lett.*, **49** (1982) 1749.
[142] Harrington S., Zhang R., Poole P. H., Sciortino F. and Stanley H. E., *Phys. Rev. Lett.*, **78** (1997) 2409.
[143] Hendricks R. W., Mardon P. G. and Shaffer L. B., *J. Chem. Phys.*, **61** (1974) 319.
[144] Kell G. S., *J. Chem. Eng. Data*, **15** (1970) 119.
[145] Waser J. and Schomaker V., *Rev. Mod. Phys.*, **25** (1953) 671.
[146] Kell G. S., *J. Chem. Eng. Data*, **15** (1970) 119.
[147] Scala A., Starr W. F., La Nave E., Stanley H. E. and Sciortino F., *Phys. Rev. E*, **62** (2000) 8016.
[148] Fuentevilla D. A. and Anisimov M. A., *Phys. Rev. Lett.*, **97** (2006) 195702.
[149] Hansen J. P. and McDonald I. R., *Theory of simple liquids* 3rd edition (Elsevier Ltd.) 2006.
[150] Stanley H. E., *Introduction to Phase Transitions and Critical Phenomena* (Oxford University Press, New York) 1971.
[151] Case D. and Manby F. R., *Mol. Phys.*, **108** (2010) 307.
[152] Vega C., Abascal J. L. F. and Nezbeda I., *J. Chem. Phys.*, **125** (2006) 34503.

[153] Komatsu T., Yoshii N., Miura S. and Okazaki S., *Fluid Phase Equilib.*, **226** (2004) 345.
[154] Guinier A. and Fournet G., *Small Angle Scattering of X-rays* (John Wiley & Sons, New York) 1955.
[155] Deem M. W. and Chandler D., *Phys. Rev. E*, **49** (1994) 4276.
[156] Soper A. K., *J. Phys.: Condens. Matter*, **17** (2005) S3273.
[157] Skinner L. B., Huang C., Schlesinger D., Pettersson L. G. M., Nilsson A. and Benmore C. J., *J. Chem. Phys.*, **138** (2013) 074506.
[158] Soper A. K., Teixeira J. and Head-Gordon T., *Proc. Natl. Acad. Sci. U.S.A.*, **107** (2010) E44.
[159] Sedlmeier F., Horinek D. and Netz R. R., *J. Am. Chem. Soc.*, **133** (2011) 1391.
[160] Yokoyama H., Kannami M. and Kanno H., *Chem. Phys. Lett.*, **463** (2008) 99.
[161] Neuefeind J., Benmore C. J., Weber J. K. R. and Paschek D., *Mol. Phys.*, **109** (2011) 279.
[162] Skinner L. B., Benmore C. J. and Parise J. B., *J. Phys.: Condens. Matter*, **24** (2012) 338001.
[163] Skinner L. B., Benmore C. J., Shyam B., Weber J. K. R. and Parise J. B., *Proc. Natl. Acad. Sci U.S.A.*, **109** (2012) 16463.
[164] Perera A., *Mol. Phys.*, **109** (2011) 2433.
[165] Hura G., Sorenson J. M., Glaeser R. M. and Head-Gordon T., *J. Chem. Phys.*, **113** (2000) 9140.
[166] Soper A. K., *Chem. Phys.*, **258** (2000) 121.
[167] Soper A. K., *J. Phys.: Condens. Matter*, **19** (2007) 335206.
[168] Fu L., Bienenstock A. and Brennan S., *J. Chem. Phys.*, **131** (2009) 234702.
[169] Hart R. T., Benmore C. J., Neuefeind J. C., Kohara S., Tomberli B. and Egelstaff P. A., *Phys. Rev. Lett.*, **94** (2005) 047801.
[170] Soper A. K., *ISRN Physical Chemistry*, **2013** (2013) 279463.
[171] Walker B. and Michaelides A., *J. Chem. Phys.*, **133** (2010) 174306.
[172] Venkatesh C. G., Rice S. A. and Narten A. H., *Science*, **186** (1974) 927.
[173] Zhang C., Khaliullin R. Z., Bovi D., Guidoni L. and Kühne T. D., *J. Phys. Chem. Lett.*, **4** (2013) 3245.
[174] Ludwig R., *Angew. Chem. Int. Ed.*, **40** (2001) 1808.
[175] Lishchuk S. V., Malomuzh N. P. and Makhlaichuk P. V., *Phys. Lett. A*, **374** (2010) 2084.
[176] Gibbs J. H., Cohen C., Fleming III P. D. and Porosoff H., *J. Sol. Chem.*, **2** (1973) 277.
[177] Mancinelli R., Botti A., Bruni F., Ricci M. A. and Soper A. K., *Phys. Chem. Chem. Phys.*, **9** (2007) 2959.
[178] Sahle C. J., Sternemann C., Schmidt C., Lehtola S., Jahn S., Simonelli L., Huotari S., Hakala M., Pylkkänen T., Nyrow A., Mende K., Tolan M., Hämäläinen K. and Wilke M., *Proc. Natl. Acad. Sci. U.S.A.*, **110** (2013) 6301.
[179] Tanaka H., *Eur. Phys. J. E*, **35** (2012) 113.
[180] Tanaka H., *J. Chem. Phys.*, **112** (2000) 799.